

This is a repository copy of Design of optimal truss components for fabrication via multiaxis additive manufacturing.

White Rose Research Online URL for this paper: <a href="https://eprints.whiterose.ac.uk/id/eprint/232768/">https://eprints.whiterose.ac.uk/id/eprint/232768/</a>

Version: Published Version

#### Article:

Lu, H. orcid.org/0000-0003-2777-3321, He, L. orcid.org/0000-0002-2537-2244, Gilbert, M. orcid.org/0000-0003-4633-2839 et al. (2 more authors) (2024) Design of optimal truss components for fabrication via multi-axis additive manufacturing. Computer Methods in Applied Mechanics and Engineering, 418. 116464. ISSN: 0045-7825

https://doi.org/10.1016/j.cma.2023.116464

#### Reuse

This article is distributed under the terms of the Creative Commons Attribution (CC BY) licence. This licence allows you to distribute, remix, tweak, and build upon the work, even commercially, as long as you credit the authors for the original work. More information and the full terms of the licence here: https://creativecommons.org/licenses/

#### Takedown

If you consider content in White Rose Research Online to be in breach of UK law, please notify us by emailing eprints@whiterose.ac.uk including the URL of the record and the reason for the withdrawal request.





Contents lists available at ScienceDirect

### Comput. Methods Appl. Mech. Engrg.

journal homepage: www.elsevier.com/locate/cma





# Design of optimal truss components for fabrication via multi-axis additive manufacturing

Hongjia Lu<sup>a</sup>, Linwei He<sup>b</sup>, Matthew Gilbert<sup>b,\*</sup>, Filippo Gilardi<sup>c</sup>, Jun Ye<sup>d</sup>

- <sup>a</sup> Centre for Innovative Structures and Materials, School of Engineering, RMIT University, Melbourne 3001, Australia
- <sup>b</sup> Department of Civil & Structural Engineering, University of Sheffield, Mappin Street, Sheffield S1 3JD, UK
- c MX3D, 1014 BK Amsterdam, The Netherlands
- <sup>d</sup> School of Civil Engineering, University of Leeds, Leeds LS2 9JT, UK

#### ARTICLE INFO

## Dataset link: https://doi.org/10.15131/shef.da ta.22559578

Keywords:
Additive manufacturing
Topology optimization
Layout optimization
Printing plan optimization

#### ABSTRACT

Additive manufacturing (AM) has developed rapidly in recent years and has the potential to enable fabrication of structurally optimized components that have hitherto been impossible to manufacture. When the degree of design freedom is high it can be observed that structurally optimized components are often truss-like in form, such that truss topology (or 'layout') optimization methods can be used to rapidly and directly identify optimal forms. However, these forms are often geometrically complex, and the presence of overhanging elements means that they generally need to be manufactured with support structures when traditional 3axis AM machines are employed. To reduce, or even completely eliminate, the need for support structures, multi-axis AM machines with 5 or more axes can instead be used. In this contribution a novel process-aware truss layout optimization strategy tailored for multi-axis AM machines is proposed, which involves combining curved printing surface identification with truss layout and geometry optimization. Due to the non-linear and non-convex nature of the resulting optimization formulation, two strategies are proposed: (i) performance-based, to obtain highly materially-efficient structures, though which have as little need for support structures as possible; (ii) printability-based, to obtain fully self-supportable structures, though which consume as little material as possible. Several examples are presented to demonstrate the effectiveness of the proposed approach. It is shown that fully self-supporting optimized structures can often be identified, with little or no sacrifice in terms of structural performance.

#### 1. Introduction

In recent years additive manufacturing (AM, also commonly referred to as '3D printing') has gradually shifted from being a rapid prototyping tool to being a large-scale automated manufacturing technology, with a range of AM methods now available for use by industry. For example, the direct energy deposition approach (DED) can be used in conjunction with multi-axis machines, defined herein as machines with 5 or more axes of motion (most usually 6 or 8 axes), including a tiltable base platform. Compared with 3-axis AM machines (e.g., those using the powder bed fusion approach), DED provides increased fabrication flexibility, speed and efficiency [1].

One challenge affecting many AM processes is the placement of material that extends outwards over a previous layer, commonly referred to as the overhang problem. This issue can be addressed by utilizing temporary support structures. However, when using

E-mail address: m.gilbert@sheffield.ac.uk (M. Gilbert).

https://doi.org/10.1016/j.cma.2023.116464

Received 4 April 2023; Received in revised form 30 August 2023; Accepted 17 September 2023

Available online 13 October 2023 0045-7825/© 2023 The Author(s). Published by Elsevier B.V. This is an open access article under the CC BY license (http://creativecommons.org/licenses/by/4.0/).

<sup>\*</sup> Corresponding author.

DED processes such as wire arc additive manufacturing (WAAM), it is usually desirable to keep the use of temporary support structures to an absolute minimum. This is because they increase material costs and deposition time [2], and can also be labour intensive and time-consuming to remove [3]. To address this problem, model decomposition (or 'segmentation') approaches can be considered; these involve separately manufacturing a series of sub-parts and then bringing these together to form the final component. However, the final assembly process generally introduces additional manufacturing costs and may also affect structural performance [4]. On the other hand, when using a multi-axis configuration, this assembly process is potentially no longer required, since all parts can be printed as part of a continuous process. This technology is therefore of growing research interest. For example, algorithms have been developed to decompose a component into zones [5–7], each of which are assigned local build directions. Also, in [2] a given 3D model is separated into overhang-free interior elements and exterior elements where overhangs are allowed. In other studies the decomposition concept has been extended by introducing curved printing surfaces, which permit different printing directions at different points of a component. For example, Dai et al. [8] developed an approach that divided a 3D voxel model into curved voxel layers to minimize the effects of the overhang problem. Xu et al. [9] extended the curved printing surface approach to be applicable to any surface mesh model, with Li et al. [10] then improving its computational efficiency by employing a geodesic distance field approach. Xie et al. [11] further extended the curved printing surface approach to ensure only convex surfaces are present, such that collisions between the printer nozzle and parts of the fabricated component are avoided. Also, Li et al. [12] considered a vector field-based approach to take support-free and collision-free conditions, together with mechanical performance, into consideration at the path planning stage. However, although the aforementioned workers proposed methods of addressing the overhang problem, they focused solely on the identification of printing surfaces for a given, predetermined, component form, which in some cases may be found to be too complex to manufacture without supports. The latter is particularly likely when components with optimized structural forms are considered.

For components manufactured via 3-axis AM machines a common approach to identify optimal or near-optimal structural forms that can be printed without supports has been to utilize topology optimization. Most often, well-known density based methods [13] have been used to achieve this. For example, in [14] the authors decomposed the optimized structure into multiple self-supporting components. In [15,16] a 45° filter function that enforced self-supporting structural forms was introduced for 2D topology optimization problems. The filter function was extended in [17,18] to allow a wider range of maximum overhang angles to be considered; in [19] the method was made even more versatile by allowing consideration of a range of element shapes. In addition to the filter approach, Qian [20] and Garaigordobil et al. [21] directly imposed overhang constraints by limiting the inclination angle of structural edges. Similarly, van de Ven et al. [22,23] used a front propagation technique to identify overhanging elements, such that these could be eliminated during the optimization process. Wang [24] considered the build direction as an additional variable in the topology optimization problem with overhang constraints, so that more efficient designs could be obtained. In addition to the density approach, the overhang problem has also been incorporated into other topology optimization formulations, such as the level-set method (e.g., Allaire et al. [25], Wang et al. [26] and Zhang and Zhou [27]), the evolutionary structural optimization approach (e.g., Bi et al. [28]), the Moving Morphable Component and Moving Morphable Void methods (e.g., Guo et al. [29]) and truss topology optimization methods (e.g., Mass and Amir [30] and He et al. [31]). These studies show that the overhang constraint problem has been quite extensively studied for 3-axis configurations. The studies have also indicated that whilst the imposition of overhang constraints may often cause relatively little performance sacrifice in a design problem with a large volume fraction (ratio between optimized structural volume and starting design domain volume), larger performance sacrifices are likely in the case of low volume fraction design problems, where truss-like forms are often identified as being optimal [25].

To obviate the need to use post-processing techniques to convert into a truss a solution obtained via continuum topology optimization methods, truss layout optimization approaches (after [32–34]) can be used to directly identify an optimal form. The use of truss layout optimization methods to design AM components has been considered previously by workers such as Smith et al. [35], Zegard and Paulino [36] and He et al. [31]; here the use of a geometry optimization rationalization step is also considered to reduce the complexity of the designs, without sacrificing performance (after He and Gilbert [37]). However, as observed by He et al. [31], relatively large performance sacrifices can be observed when fabricating truss structures using 3-axis AM machines unless temporary support structures are employed. To help address this, in the present contribution multi-axis AM machines are instead employed. Also, to properly realize the potential of multi-axis AM machines, it is of interest to consider the holistic optimization problem in which printing surface identification and component design optimization are considered simultaneously, noting that, when multi-axis AM machines are used, curved, rather than horizontal, printing surfaces can be employed. Since the resulting holistic optimization problem is non-linear and non-convex, two approaches are here proposed, prioritizing either performance or printability. In the former case the aim is to maximize the material-efficiency of the structure, while also keeping the need for support structures low. In the latter case the aim is to generate structures that are completely self-supporting, while also keeping material-efficiency high.

The paper is organized as follows. Section 2 describes a means of identifying the curved printing surfaces associated with multi-axis AM for a given structural component of predetermined form, whilst Section 3 describes a holistic optimization approach capable of simultaneously identifying suitable printing surfaces and optimal structural layout. The efficacy of the approach is then demonstrated via application to example problems in Section 4. Finally, conclusions from the work are drawn in Section 5.

#### 2. Printing surface identification for multi-axis additive manufacture

#### 2.1. Multi-axis additive manufacture

The present work focuses on additive manufacture (AM) using multi-axis DED machines. In such a machine a printing nozzle is usually attached to a robot arm, as shown in Fig. 1(a). Arising from the overhang problem mentioned in the previous section, the

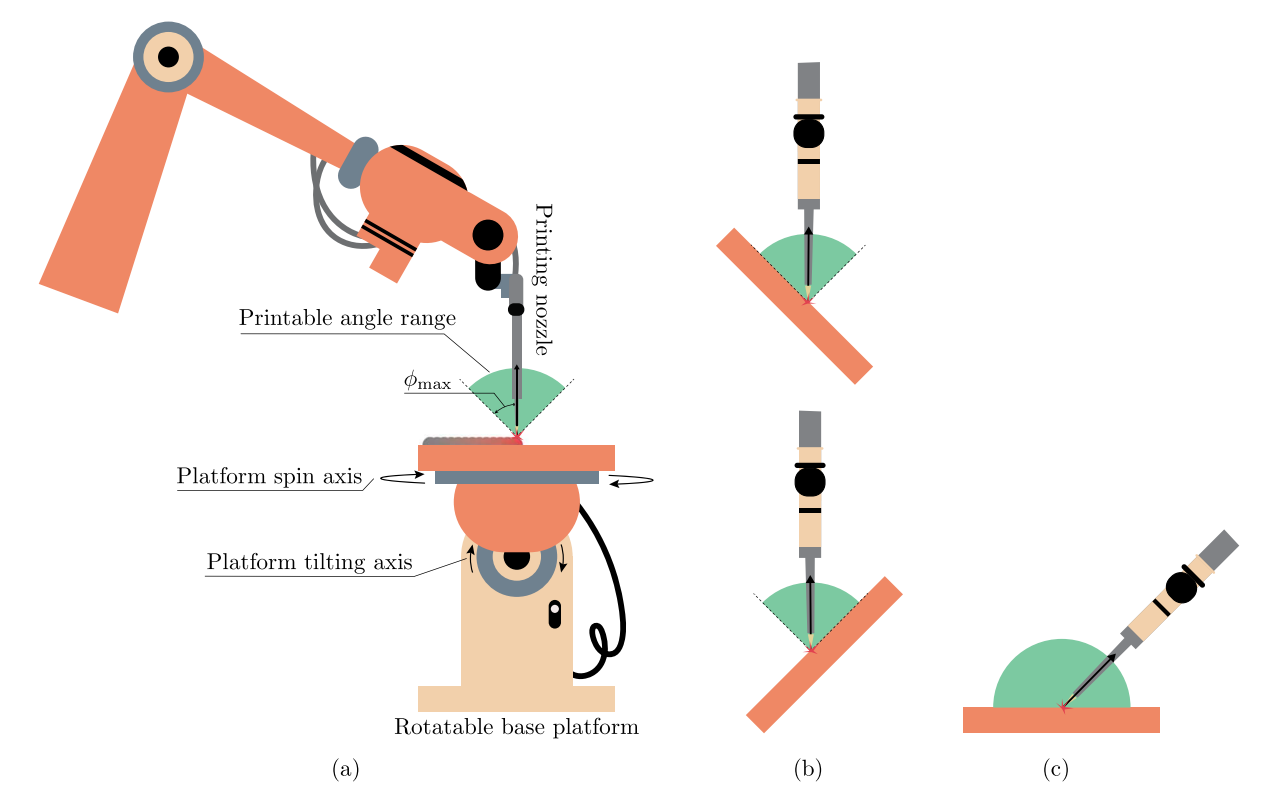


Fig. 1. Multi-axis AM configuration: (a) DED machine with machine arm and rotatable base platform; (b) the printable angle range when the base platform is tilted; (c) expanded printable range due to base platform tilt capability (note that a 180° range will not always be reachable due to the potential for collision between the printing nozzle and the base platform).

maximum printable angle for a printing surface (i.e.,  $\phi_{max}$  in Fig. 1(a)) is limited. However, taking advantage of rotatability of the base platform, the maximum effective printable angle range can be extended; see Fig. 1(b) and (c).

A consequence of the ability of the printing nozzle and/or base platform to tilt is that the printing surface no longer needs to remain horizontal, and can become curved. To illustrate the concept, Fig. 2(a) and (b) show planar and curved printing surfaces. Although the maximum printable angle limitation remains the same (see green regions in Fig. 2(a) and (b)), the use of curved printing surfaces significantly increases flexibility, for example permitting manufacture of components with elements inclined at shallow angles to the base platform, thereby helping to address the overhang problem. Note that, even though printing surfaces can be curved, the primary build direction remains unchanged (i.e., from bottom to top in Fig. 2). Thus the choice of primary build direction will still influence the printing process, as will be discussed later.

Although the use of curved printing surfaces provides a potential means of addressing the overhang problem, other issues can arise. For example, as shown in [9], concave surfaces can lead to potential collisions between the printing head and already printed elements, as shown in Fig. 2(c). To avoid this, the turning angle,  $\phi_t$ , should be sufficiently small, as shown in Fig. 2(d).

It is also worth noting that curved printing surfaces need not necessarily be smooth or continuous. In fact the entire domain can be divided into zones, each of which has a single local build direction, e.g., see Fig. 2(e), with a caveat being that the turning angle  $\phi_t$  between zones needs to be sufficiently small to avoid collisions between the printing head and already printed elements. (There may also be hardware-specific limitations on the speed at which the nozzle can be re-orientated, such that sudden changes in angle may not always be feasible in practice.)

#### 2.2. Identification of curved printing surfaces

#### 2.2.1. Domain discretization

To maximize printability, suitable printing surfaces can be identified by referring to the structural form to be manufactured. For sake of simplicity, herein piecewise linear printing surfaces are used. Firstly, the domain is divided into a number of zones; Fig. 3 shows a simple domain divided into four zones. Secondly, by analysing the orientations of the structural members present within each zone, suitable local build directions are determined (Fig. 3(b)). Thirdly, a series of printing surfaces are created (Fig. 3(c)). Since the curved printing surfaces are approximated via piece-wise linear surfaces, a suitably large number of zones needs to be used, with the extents and locations of zones determined via optimization; see Section 2.2.4. Once the printing surfaces are identified, appropriate base platform orientations can be determined (Fig. 3(d-h)). Note that in the simple example shown in Fig. 3, due to the

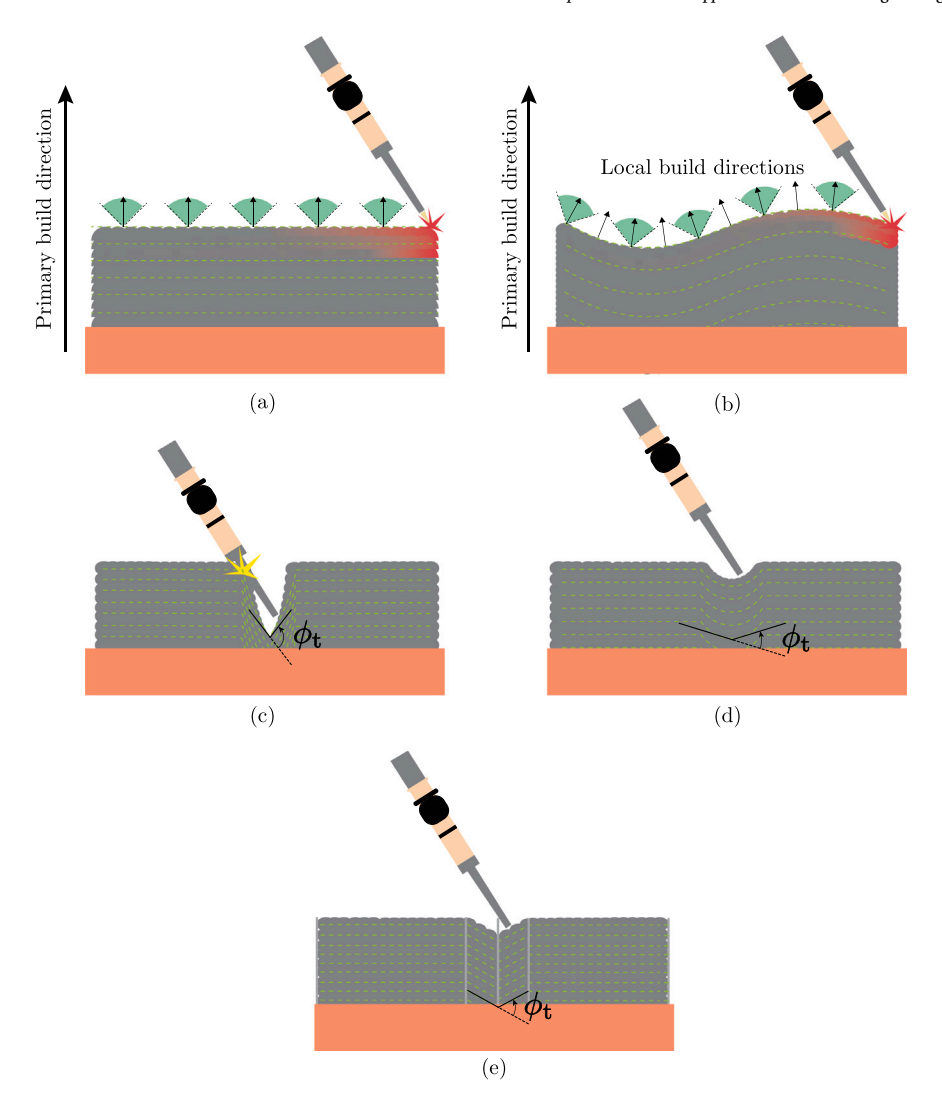


Fig. 2. Horizontal and curved printing surfaces: (a) planar (horizontal) printing surfaces and associated printable build angle ranges; (b) curved printing surfaces with associated printable build angle ranges; (c) potential collision between printing head and already printed elements when using a concave printing surface and a large turning angle  $\phi_t$ ; (d) no collision occurs when the turning angle  $\phi_t$  is small; (e) division of domain into zones possessing piece-wise linear printing surfaces (printing surfaces indicated by green dashed lines; for interpretation of the references to colour in this figure caption, the reader is referred to the web version of this article).

near-horizontal member orientations in Zones (2, 1) and (2, 2), a high turning angle  $\phi_t$  is required, indicating that a sharp nozzle would be necessary to ensure collision-free printing; the latter is discussed further in Section 2.2.3.

#### 2.2.2. Local build direction

To identify a suitable local build direction for each zone, the orientations of structural members need to be taken into account. For the single member shown in Fig. 4(a), it is clear that it is printable for any  $\phi \in [\theta - \phi_{\text{max}}, \theta + \phi_{\text{max}}]$ , where  $\phi$  and  $\theta$  are, respectively, the local build direction angle and the angle of inclination of the member, measured relative to the  $x^+$  axis. Also,  $\phi_{\text{max}}$  is the maximum permitted overhang angle. If more than one member is considered (e.g., see Fig. 4(b)), a suitable local build direction angle for a zone can be determined by minimizing the total overhang violation:

$$\min_{\phi,\eta} \quad \sum_{i \in \mathbb{M}} \eta_i \tag{1a}$$

s.t. 
$$\eta_i = |\phi - \theta_i - \phi_{\text{max}}| + |\phi - \theta_i + \phi_{\text{max}}| - 2\phi_{\text{max}}, \forall i \in \mathbb{M},$$
 (1b)

where  $\eta_i$  and  $\theta_i$  are respectively the overhang violation and orientation angle of member i;  $\mathbb{M}$  is a set containing all members passing through the given zone. Note that the objective function in (1) may not always reach zero, since it may not always be possible to

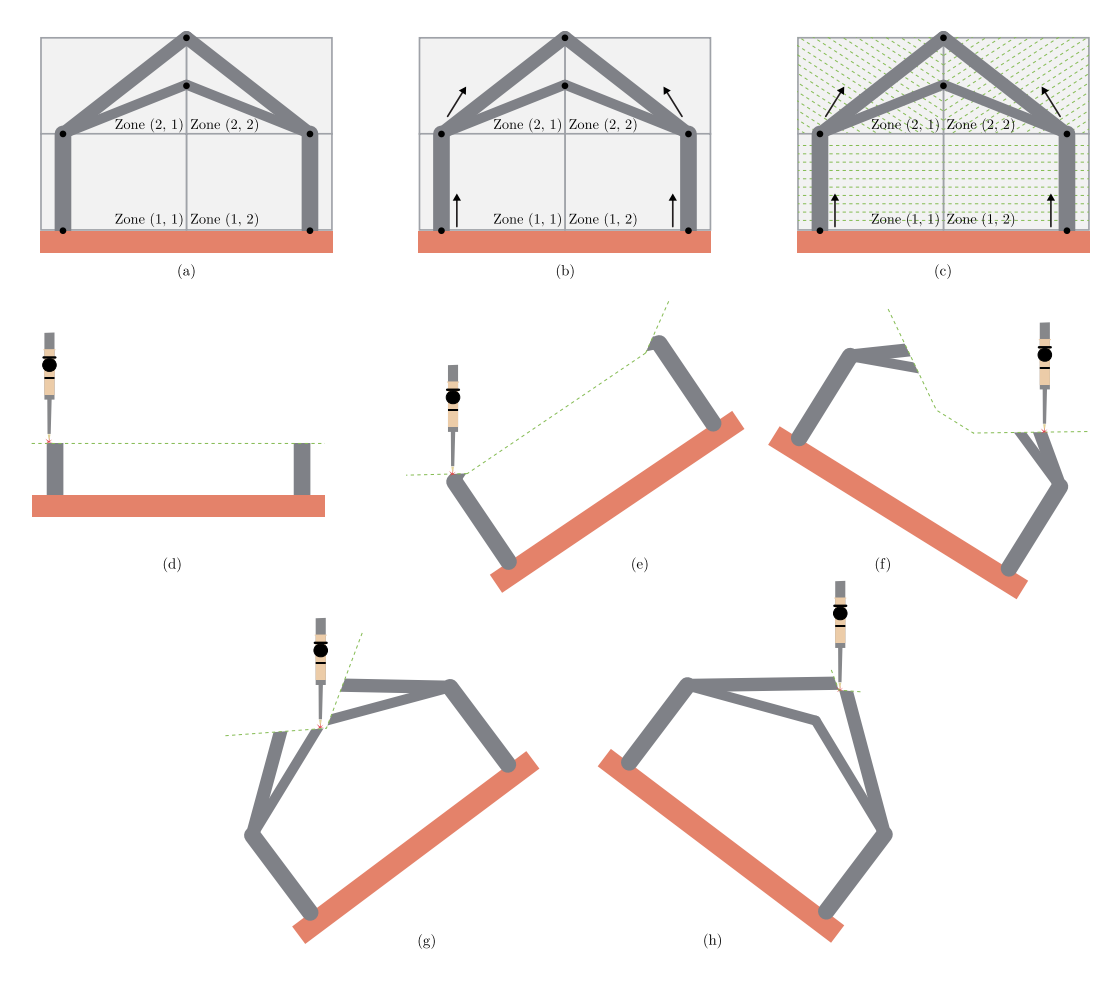


**Fig. 3.** Discretizing a domain with zones for printing surface identification: (a) the design domain is discretized into four zones; (b) local build directions are determined for each zone; (c) printing surfaces are determined based on local build directions; (d-h) base platform orientations following the printing surfaces in (c) (where zone ( $\mu$ ,  $\nu$ ) represents the zone on the  $\mu$ th row and  $\nu$ th column; arrows represent local build directions and green dashed lines represent printing surfaces; for interpretation of the references to colour in this figure caption, the reader is referred to the web version of this article).

identify a suitable local build direction; e.g., see Fig. 4(c). In this case, the most 'important' members should be prioritized, where herein the overhang violation is weighted by member volume, such that the objective function in (1) is modified to:

$$\min_{\boldsymbol{\phi}, \boldsymbol{\eta}} \quad \boldsymbol{\eta}^{\mathrm{T}} \mathbf{la}, \tag{2}$$

where  $\eta = [\eta_1, \eta_2, \dots \eta_m]$  is the member overhang violation vector with m denoting the number of members;  $\mathbf{l} = (l_{i,i}), \forall i \in \mathbb{M}$  is a  $m \times m$  matrix with member lengths on the diagonal, where  $l_{i,i} = l_i$  is the length of the ith member. Also  $\mathbf{a} = (a_i), \forall i \in \mathbb{M}$  is a vector containing member areas.

#### 2.2.3. Collision at concave printing surface

Given the local printing directions, printing surfaces can be generated by creating a series of parallel line segments perpendicular to the printing directions within each zone. However, as mentioned in Section 2.1, collision can occur at concave printing surfaces (e.g., see Fig. 2(c)). To prevent this, the turning angle  $\phi_t$  between surfaces from two adjacent zones is restricted:

$$\phi_{\rm t} \le \phi_{\rm t.max},\tag{3}$$

where  $\phi_t$  is the difference in the building angle  $\phi$  between any two adjacent segments of the printing surface;  $\phi_{t,max}$  is a predefined maximum turning angle to prevent collision. For printing nozzles with a relatively sharp shape, the risk of collision is reduced, allowing for a relatively high  $\phi_{t,max}$ . Conversely, a blunt-shaped nozzle necessitates the use of a lower  $\phi_{t,max}$ . When  $\phi_{t,max} = 0$ , the printing surface can only be horizontal or convex, ensuring collision-free printing irrespective of nozzle shape. Note that Constraint (3) effectively provides a simplified means of minimizing the risk of collision during the structural design phase. However, for comprehensive identification and elimination of collision risks, a thorough collision assessment is required (e.g. see videos that show complete simulation of the build process in the case of two of the example problems considered later in this paper).

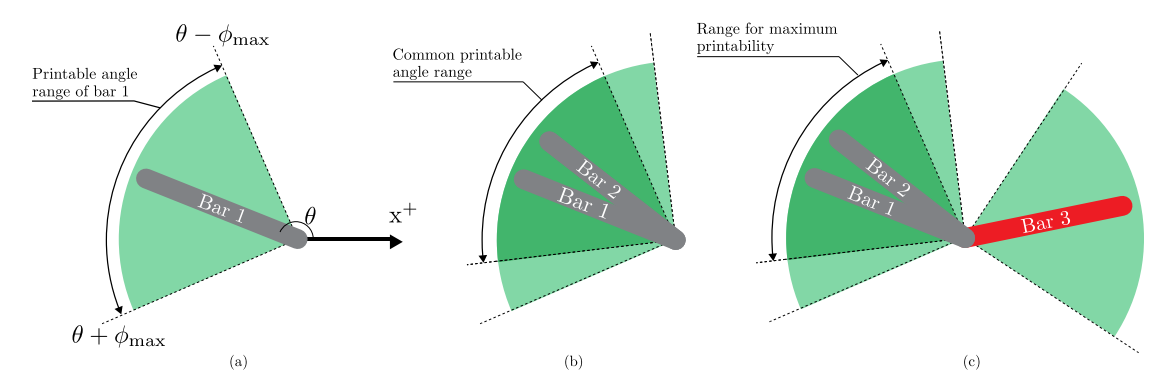


Fig. 4. Printable angle ranges for members: (a) Bar 1 is printable for any  $\phi \in [\theta - \phi_{\max}, \theta + \phi_{\max}]$ ; (b) Bar 1 and 2 are both printable as the local build direction angle can be selected from a range; (c) no local build direction angle can be found in this case (where  $\phi$  and  $\theta$  are, respectively, angles of the printing direction and the member, measured relative to the  $x^+$  axis;  $\phi_{\max}$  is the maximum permitted overhang angle).

#### 2.2.4. Problem formulation

Considering (1), (2) and (3), and assuming that the domain is discretized with  $n_{\mu} \times n_{\nu}$  zones, the optimal printing surfaces for a given truss structure can be identified by solving the following optimization problem:

$$\min_{\boldsymbol{\phi}, \boldsymbol{\eta}} \quad \sum_{\mu} \sum_{\nu} \boldsymbol{\eta}_{\mu, \nu}^{T} \mathbf{1}_{\mu, \nu} \mathbf{a}_{\mu, \nu}$$
s.t. 
$$\boldsymbol{\eta}_{\mu, \nu} = |\phi_{\mu, \nu} \mathbf{e} - \theta_{\mu, \nu} - \phi_{\text{max}} \mathbf{e}| + |\phi_{\mu, \nu} \mathbf{e} - \theta_{\mu, \nu} + \phi_{\text{max}} \mathbf{e}| - 2\phi_{\text{max}} \mathbf{e}, \forall \mu \in \mathbb{Z}_{\mu}, \forall \nu \in \mathbb{Z}_{\nu}$$

$$\boldsymbol{\phi}_{t} \leq \phi_{t \text{ max}} \mathbf{e}, \tag{4}$$

where  $n_{\mu}$  and  $n_{\nu}$  are the numbers of rows and columns of zones used in domain discretization shown in Fig. 3, where  $\mu$  and  $\nu$  are used for row and column indices, respectively.  $\mathbb{Z}_{\mu} = \{1, 2, \dots, n_{\mu}\}$  and  $\mathbb{Z}_{\nu} = \{1, 2, \dots, n_{\nu}\}$  are sets containing row and column indices of zones, respectively. Also,  $\eta_{\mu,\nu}$ ,  $\mathbf{a}_{\mu,\nu}$  and  $\theta_{\mu,\nu}$  are vectors containing, respectively, overhang violations, areas and orientation angles of members in the zone at the  $\mu$ th row and  $\nu$ th column, where  $\mathbf{I}_{\mu,\nu}$  is a diagonal matrix of lengths of the members, and  $\phi_{\mu,\nu}$  is the building direction of the zone. And  $\mathbf{e} = [1,1,\dots]^T$  is an all-one vector with appropriate length, and  $\phi_t = [\phi_{1,2} - \phi_{1,1}, \phi_{1,3} - \phi_{1,2}, \dots, \phi_{\mu,\nu} - \phi_{\mu,\nu-1}, \dots, \phi_{n_{\mu},n_{\nu}} - \phi_{n_{\mu},n_{\nu}-1}]^T$  is a vector containing turning angles between adjacent zones in any row. In this problem, the printing surface parameters,  $\phi$  and  $\eta$ , are variables, while the structure parameters,  $\mathbf{l}$ ,  $\mathbf{l}$ , and  $\theta$ , along with the printing configuration parameters,  $\phi_{\text{max}}$  and  $\phi_{\text{t,max}}$ , remain constant. Given that both the objective function and the constraints are linear, Problem (4) is a linear programming (LP) problem, which can be solved efficiently using a modern commercial LP solver, e.g., Mosek [38]. Moreover, in this case a globally optimal solution is obtained.

#### 2.2.5. Example

To show the capability of the proposed algorithm to generate printing surfaces for a given structure, a simple example involving a truss comprising solid members is tackled. For the structure shown in Fig. 5(a), it is assumed that a fixed vertical primary build direction will be used and that  $\phi_{max} = 45^{\circ}$  and  $\phi_{t,max} = 45^{\circ}$ . Four zones are employed, splitting the structure into four parts, Fig. 5(b). Then Problem (4) is solved to identify local building directions, Fig. 5(c). Finally, printing surfaces are generated in Fig. 5(d). Note that in Fig. 5(d), the highlighted member on the top is still not printable due to the violation shown in Fig. 4(c). Nevertheless, its printability has been improved relative to that possible using 3-axis AM. Although in this case other primary build directions could be used to improve printability, in general more advanced techniques are needed to achieve this, which will be introduced in the next section.

#### 3. Simultaneous printing surface identification and truss optimization formulation

#### 3.1. Overview

Although multi-axis AM can improve the printability of a structure, its potential can be more fully realized when it is used in combination with structural optimization; Fig. 6 illustrates the various options available, considering both 3-axis and multi-axis additive manufacture:

- In (A), a conventional structure is directly manufactured using 3-axis AM. Depending on the form of the structure, its printability and performance may be low.
- · Approach (B) is similar to (A), though multi-axis AM is now used, increasing printability.
- In (C), the structure is optimized first to achieve better performance. However, depending on its form, printability may be low.

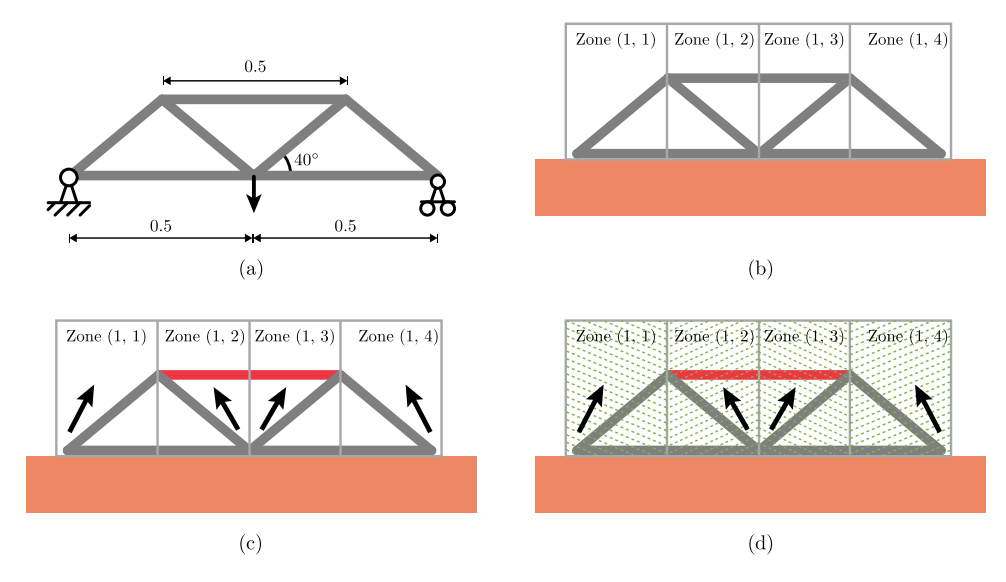


**Fig. 5.** Multi-axis printing plan: (a) conventional truss structure design; (b) domain discretized into 4 zones; (c) local build directions identified for each zone; (d) printing surfaces are determined from the local build directions (where Zone  $(\mu, \nu)$  represents the zone on the  $\mu$ th row and  $\nu$ th column; arrows represent local build directions; red bars are not printable; green dashed lines represent printing surfaces; for interpretation of the references to colour in this figure caption, the reader is referred to the web version of this article)

- In (D), multi-axis AM is used to fabricate the optimized structure, increasing printability.
- In (E), the structure is generated via a holistic optimization considering the constraints associated with the 3-axis AM process. Although printability is good in this case, this is at the expense of structural performance.
- In (F), multi-axis AM offers more design freedom in the holistic approach. Good printability and performance are therefore both achievable.

Approaches (A), (C) and (E) can be achieved via established 3-axis AM methods (see, e.g., Mass and Amir [30] and He et al. [31]). Techniques in Fig. 5 will improve printability when using approaches (B) and (D). However, to fully exploit the power of multi-axis AM, a holistic optimization is needed to achieve (F), which will be introduced later in this paper. However, first the basic truss layout optimization formulation will be revisited.

#### 3.2. Basic truss layout optimization formulation

Numerical truss layout optimization methods [32–34] provide a powerful means of generating highly efficient truss-like structures with given conditions (e.g., domain, load and support conditions etc). The standard process involves a series of steps, as shown in Fig. 7(a–c). Firstly, the design domain, load and support conditions are specified, Fig. 7(a); secondly, nodes are generated inside the design domain and potential members are created by interconnecting these nodes, Fig. 7(b), forming a 'ground structure'; finally, the optimal layout is identified (Fig. 7(c)) by solving the following problem:

$$\min_{\mathbf{a},\mathbf{a}} V = \mathbf{l}^{\mathbf{T}}\mathbf{a} \tag{5a}$$

s.t. 
$$\mathbf{Bq} = \mathbf{f}$$
 (5b)

$$-\sigma_c \mathbf{a} \le \mathbf{q} \le \sigma_t \mathbf{a} \tag{5c}$$

$$\mathbf{a} \ge 0,\tag{5d}$$

where V represents total structure volume;  $\mathbf{l} = [l_1, l_2, \dots, l_m]^{\mathrm{T}}$  is a vector of member lengths with m denoting the number of members;  $\mathbf{a} = [a_1, a_2, \dots, a_m]^{\mathrm{T}}$  is a vector containing the member cross-sectional areas;  $\mathbf{q} = [q_1, q_2, \dots, q_m]^{\mathrm{T}}$  is a vector containing the internal member forces;  $\mathbf{f} = [f_{1x}, f_{1y}, f_{2x}, f_{2y}, \dots, f_{nx}, f_{ny}]^{\mathrm{T}}$  is a vector containing the external forces applied on nodes, with n denoting the number of nodes. Also  $\sigma_t$  and  $\sigma_c$  are limiting tensile and compressive stresses respectively.  $\mathbf{B}$  is a  $2n \times m$  equilibrium matrix comprising direction cosines. Note that in this formulation, the member-related parameters  $\mathbf{q}$  and  $\mathbf{a}$  are design variables, while the node position dependent parameters,  $\mathbf{l}$  and  $\mathbf{B}$ , and the load vector  $\mathbf{f}$  and material stress limit  $\sigma_c$  and  $\sigma_t$  parameters, remain constant. Therefore, Problem (5) is a LP problem. Further details of the traditional truss layout optimization can be found e.g., in [33,34].

Building on the traditional truss layout optimization formulation, in [31] an approach to design self-supporting structures for 3-axis machines was proposed, where in this case the printing platform cannot move (i.e, tilt or spin). For this reason, the permitted building directions are fixed (e.g., Fig. 2(a)), and thus are uncoupled from the optimization problem. However, multi-axis machines

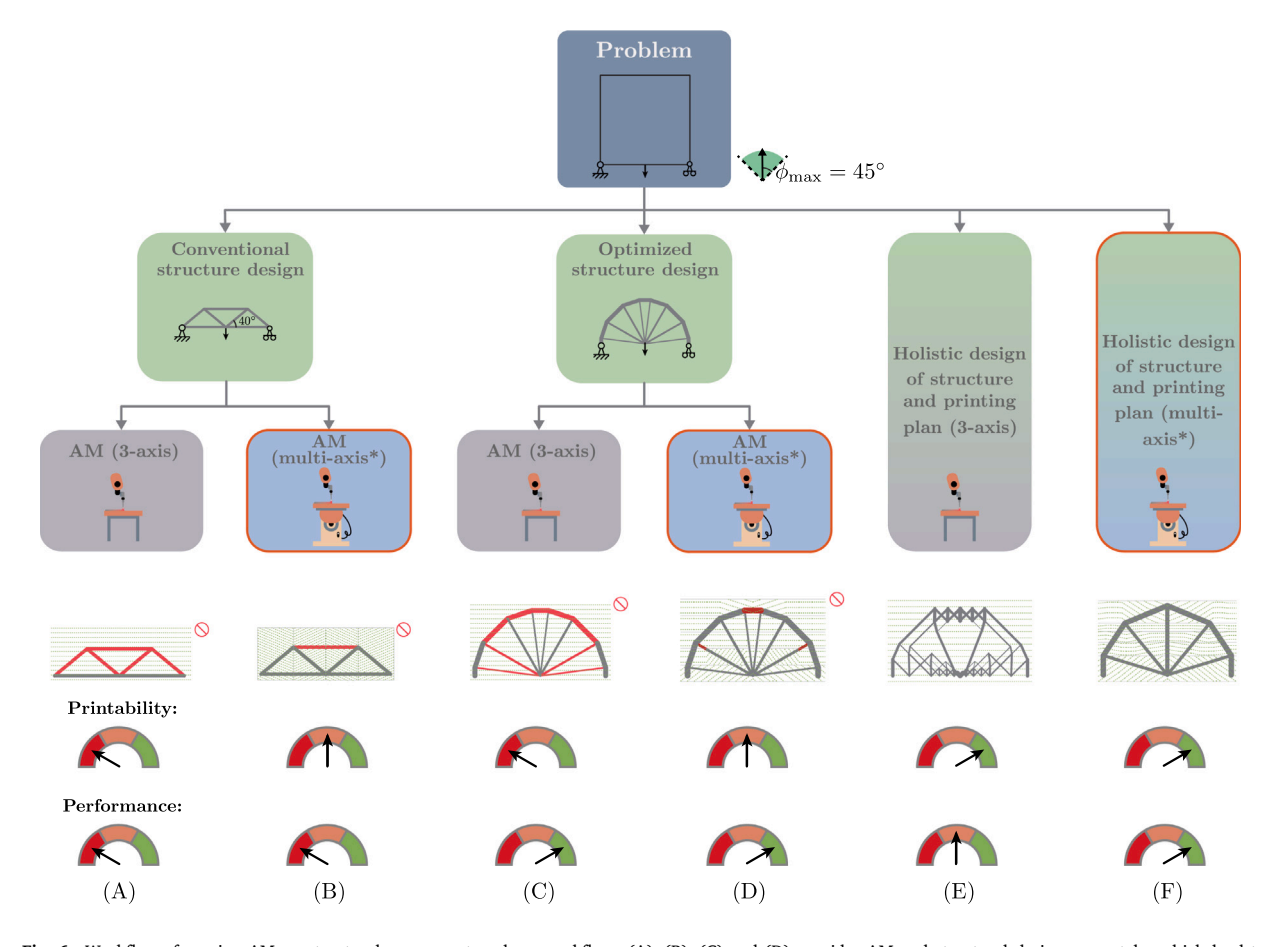


Fig. 6. Workflows for using AM on structural components, where workflows (A), (B), (C) and (D) consider AM and structural design separately, which lead to not fully printable structures; workflows (E) and (F) design AM printing plan and structure simultaneously (\*multi-axis represents machines with 5- or more-axis configuration; green dashed lines represent printing surfaces; red bars are unprintable due to overhang;  $\phi_{max} = 45^{\circ}$  is used; for interpretation of the references to colour in this figure caption, the reader is referred to the web version of this article).

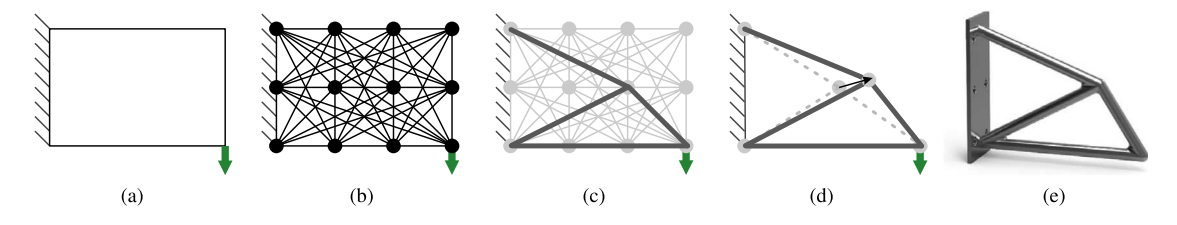
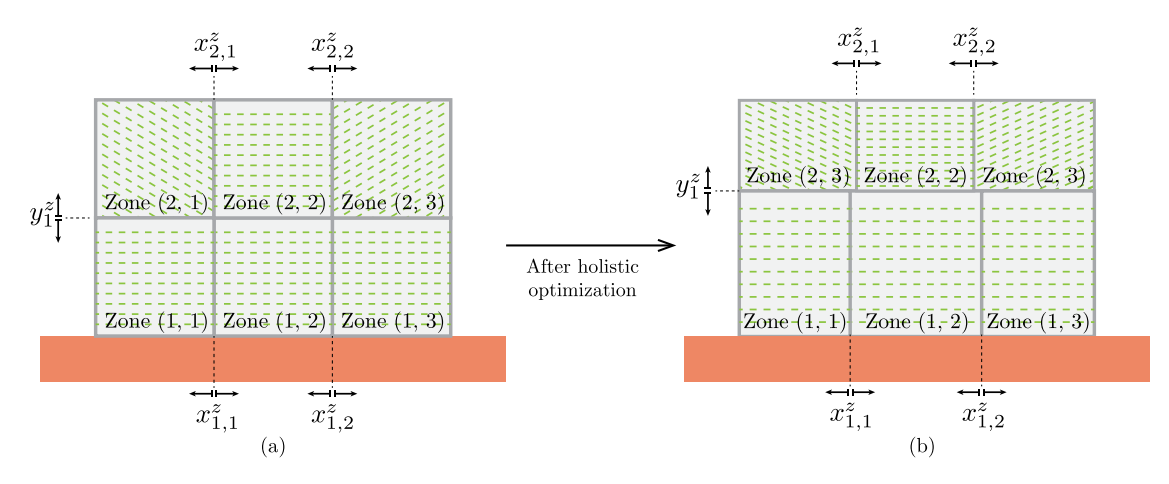


Fig. 7. Steps in the layout optimization approach for AM components [31]: (a) specify design domain, loads and supports; (b) discretize domain using nodes and interconnect these with potential members, forming a 'ground structure'; (c) use the layout optimization formulation to identify the subset of members forming the optimal structure; (d) use geometry optimization to rationalize the structure; (e) convert to solid 3D model ready for AM.

allow variable building directions (e.g., Fig. 2(b)), so in this work the printing surface identification process described in Section 2.2 can potentially be considered in conjunction with truss layout optimization, giving rise to a holistic problem formulation.

#### 3.3. Holistic printing surface identification/truss optimization formulation

As mentioned earlier, a significant benefit of using multi-axis machines lies in the fact that the printing surfaces can become curved, allowing members at shallow angles to the building platform to be manufactured (e.g., Fig. 3). As shown in Section 2.2, the design domain is divided into zones, within which the directions of the printing surfaces are determined. Since the quality of the solutions obtainable will be influenced by how these zones are arranged, it is beneficial to make the size and position of each



**Fig. 8.** Zones with optimizable boundaries defined by  $x_{\mu,\nu}^z$  and  $y_{\mu}^z$ : (a) initial locations and sizes of zones; (b) optimized zones (zone ( $\mu,\nu$ ) represent the zone on the  $\mu$ th row and  $\nu$ th column and green dashed lines represent printing surfaces (for interpretation of the references to colour in this figure caption, the reader is referred to the web version of this article).

zone adjustable; see Fig. 8. Therefore, to simultaneously optimize structural layout and printing surfaces, the following holistic optimization problem can be formulated:

$$\min_{\substack{\mathbf{a}, \phi, \eta, \\ \mathbf{x}, \mathbf{y}, \mathbf{z}' \mathbf{y}'}} \mathbf{1}^{\mathbf{T}} \mathbf{a} \tag{6a}$$

s.t. 
$$\mathbf{Bq} = \mathbf{f}$$
 (6b)

$$-\sigma_{r}\mathbf{a} \leq \mathbf{q} \leq \sigma_{r}\mathbf{a}$$
 (6c)

$$\phi_{\rm t} \le \phi_{\rm t.max}$$
 (6d)

$$\sum_{\mu} \sum_{\nu} \mathbf{\eta}_{\mu,\nu}^{\mathrm{T}} \mathbf{I}_{\mu,\nu} \mathbf{a}_{\mu,\nu} \le \epsilon \tag{6e}$$

$$\boldsymbol{\eta}_{\mu,\nu} = |\phi_{\mu,\nu} \mathbf{e} - \theta_{\mu,\nu} - \phi_{\text{max}} \mathbf{e}| + |\phi_{\mu,\nu} \mathbf{e} - \theta_{\mu,\nu} + \phi_{\text{max}} \mathbf{e}| - 2\phi_{\text{max}} \mathbf{e}, \forall \mu \in \mathbb{Z}_{\mu}, \forall \nu \in \mathbb{Z}_{\nu}$$
(6f)

$$\mathbf{a} \ge 0,$$

where  $\mathbf{x} = [x_1, x_2, \dots, x_n]^T$  and  $\mathbf{y} = [y_1, y_2, \dots, y_n]^T$  are vectors of node x- and y-coordinates with n denoting the number of nodes;  $\mathbf{x}^z = [x_{1,1}^z, x_{1,2}^z, \dots, x_{\mu,\nu}^z, \dots, x_{n_\mu-1,n_\nu-1}^z]^T$  and  $\mathbf{y}^z = [y_1^z, y_2^z, \dots, y_\nu^z, \dots, y_{n_\nu-1}^z]^T$  are vectors containing, respectively, vertical and horizontal positions of zone boundaries. Also,  $\epsilon$  is a small positive number introduced to avoid numerical issues.

In order to prevent zones from reducing in size to below a set threshold (and potentially leading to a large turning angle  $\phi_t$ , e.g., see Fig. 2(c)), the following constraints are introduced:

$$x_{\mu,\nu}^{\mathbf{z}} - x_{\mu,\nu-1}^{\mathbf{z}} \ge \delta_{\mathbf{x}}, \quad \forall \mu \in \mathbb{Z}_{\mu}, \forall \nu \in \overline{\mathbb{Z}}_{\nu}$$
 (7a)

$$y_{\mu}^{z} - y_{\mu-1}^{z} \ge \delta_{y}, \quad \forall \mu \in \overline{\mathbb{Z}}_{\mu},$$
 (7b)

where  $\overline{\mathbb{Z}}_v = \{2, 3, \dots, n_v - 1\}$  and  $\overline{\mathbb{Z}}_u = \{2, 3, \dots, n_u - 1\}$  are the indices vector for the concerned zone boundaries.

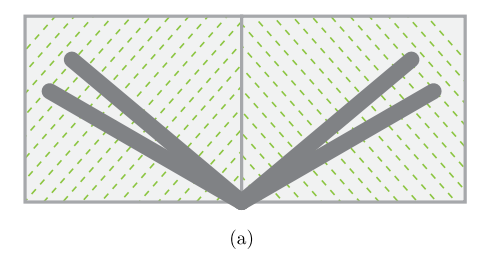
As mentioned in Section 2.2, the printing surfaces are determined using member directions within zones. However, the optimization process may move members into different zones (e.g., see Fig. 9), making it challenging to determine suitable printing surface locations without introducing discrete variables. Hence, for sake of simplicity, here members are restricted to lie within their initially assigned zones in the geometry optimization step. Firstly, members are split using the zone boundaries so that each member segment then lies entirely within a single zone (i.e., no member segment passes through two or more zones). Secondly, the end nodes of member segments are restricted using:

$$x_{\mu,\nu-1}^{\mathbf{z}} \mathbf{e} \le \mathbf{x}_{\mu,\nu} \le x_{\mu,\nu}^{\mathbf{z}} \mathbf{e} \tag{8a}$$

$$y_{u-1}^{\mathbf{z}} \mathbf{e} \le \mathbf{y}_{u,v} \le y_{u}^{\mathbf{z}} \mathbf{e},\tag{8b}$$

where  $\mathbf{x}_{\mu,\nu}=(x_i), \forall i\in\mathbb{N}_{\mu,\nu}$  and  $\mathbf{y}_{\mu,\nu}=(y_i), \forall i\in\mathbb{N}_{\mu,\nu}$  are the x- and y- coordinate vectors for all end nodes of member segments within zone  $(\mu,\nu)$ ;  $\mathbb{N}_{\mu,\nu}$  is a set containing indices of nodes within the zone.

Problem (6) is non-linear and non-convex, so the starting points are of importance [39]. An initial guess of the printing surface can be obtained by solving (4), using a structural layout obtained from (5). However, an inappropriate initial distribution of zones may lead to the same situation in Fig. 9(b), which will create numerical difficulties for the holistic optimization. Therefore, in certain



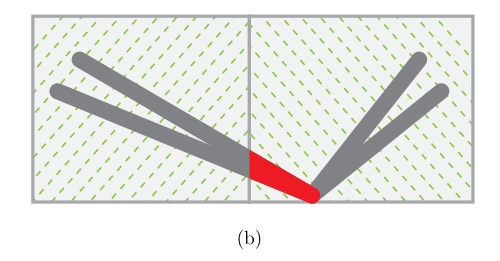


Fig. 9. Incorrect node movement making part of the structure unprintable: (a) initial structure; (b) potential optimized structure if Constraints (8a) and (8b) are not applied (unprintable area highlighted in red; green dashed lines represent printing surfaces; for interpretation of the references to colour in this figure caption, the reader is referred to the web version of this article).

examples (see Section 4), the initial distribution of zones is manually adjusted to split truss structures at their joints. To generate a starting structure for (6), two approaches are developed, prioritizing either structural performance (using an exterior starting point), or printability (using an interior starting point).

#### 3.3.1. Prioritizing structural performance (exterior starting point)

To prioritize structural performance, Problem (6) can be relaxed so as to be convex, such that a global optimum can be generated and then used as a starting point. Since the solution from a relaxed convex problem is a strict lower bound of (6), this starting point can prioritize structural performance, with, for the sake of simplicity, (5) used as the relaxed problem. Note that, since starting points are generated by relaxing constraints, some constraint in the full Problem (6) are likely to be violated. To address this, instead of directly imposing constraint (6e), it is included in penalized form in the objective function:

$$\min_{\substack{\mathbf{a},\mathbf{q},\boldsymbol{\phi},\boldsymbol{\eta},\\\mathbf{x},\mathbf{y},\mathbf{x}^2,\mathbf{y}^2}} \mathbf{l}^{\mathbf{T}}\mathbf{a} + p(\sum_{\mu} \sum_{\nu} \boldsymbol{\eta}_{\mu,\nu}^{\mathbf{T}} \mathbf{l}_{\mu,\nu} \mathbf{a}_{\mu,\nu}), \tag{9}$$

where p is a sufficiently large penalty factor (taken as  $100V_0$  in this paper, where  $V_0$  is the volume of the structure from problem (5)). The penalization term, i.e.,  $p(\sum_{\mu} \sum_{\nu} \mathbf{\eta}_{\mu,\nu}^{\mathsf{T}} \mathbf{1}_{\mu,\nu} \mathbf{a}_{\mu,\nu})$ , can be viewed as additional costs associated with manufacturing support structures. This approach is similar to the 'soft constraint' used in [31], with the optimization starting with an exterior starting point in which overhang violations are allowed. Although the optimization process will reduce overhang violations, it does not guarantee that the resulting optimized structures will be fully self-supported. Nevertheless, with the increased design freedom associated with printing surface optimization, in many cases the penalization term can be reduced so as to become negligible after solving (9).

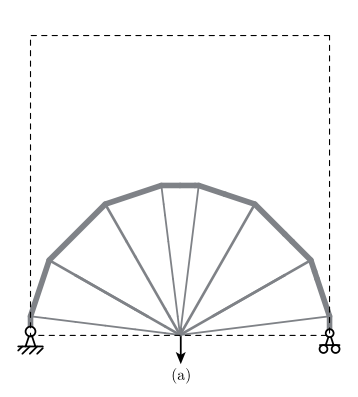
#### 3.3.2. Prioritizing printability (interior starting point)

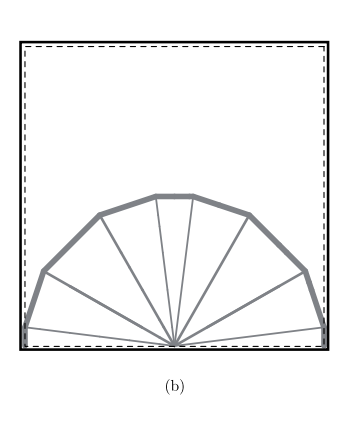
To prioritize printability, constraint (6e) has to be strictly satisfied. Given the initial printing surfaces, structural members violating the angle constraint (i.e., members with  $\eta > 0$ ) can be removed from the ground structure. Note that, for zones without structural members, horizontal printing surfaces are used. When all violated members are removed, Eq. (5) is solved for the second time to generate a self-supporting structural layout. This approach is similar to the 'hard constraint' approach considered in [31], where the optimization process now begins with an interior starting point without overhang violation. However, here an initial guess of the printing surfaces is required; clearly, the selection of initial structural layout, and hence initial printing surfaces, will influence the subsequent optimization. This is therefore identified as an area requiring further work. Also note that, due to the removal of members from the ground structure, the volume of the interior starting point is likely to be relatively high; however, given the increased design freedom provided in the printing surface identification step, it is likely that the structural efficiency can be significantly improved after solving Eq. (6).

#### 4. Numerical examples

To demonstrate the effectiveness of the proposed methods, several design examples are now considered. The linear optimization Problem (5) is solved via Mosek [38], while the non-linear optimization problem (6) is solved using IPOPT (Wächter and Biegler [40]), following the geometry optimization framework introduced in [37]. Unless specified otherwise, the material used is an aluminium alloy (AlSi<sub>10</sub>Mg) with an allowable compressive and tensile stress of 255 MPa. Also, for sake of simplicity, domain restrictions are only enforced on a centreline basis in the optimization process (see Fig. 10(a)); if a strict domain restriction is required (e.g., see Fig. 10(b)), the approach described in Section 4.2 of He et al. [31] can be used. Here, for the printing surface identification step, a domain that is large enough to cover all parts of all structural members is used (Fig. 10(c)).

Note that 3D models of the structures are generated using the approach described in [35]. Although the basic truss layout optimization formulation assumes pin joints, some joint rigidity will inevitably be present when a structure is additively manufactured, such that some bending stresses will be induced when the structure is loaded. However, for problems with a high degree of design freedom (i.e., when the final optimized structure will occupy only a very small proportion of the design domain) the induced bending moments and associated bending stresses will be relatively small. Also, moment redistribution will occur at the ultimate limit state if the structure is formed from a ductile material, mitigating the issue [41]. Thus, for the sake of simplicity, bending stresses are ignored in this study.





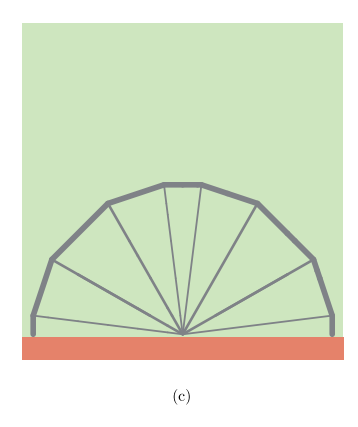


Fig. 10. Definition of design domains: (a) structural optimization design domain (i.e. dashed line), where domain restrictions are enforced on a member centreline basis; (b) enlarged design domain (i.e., solid line), with domain restrictions enforced on a model boundary basis; (c) domain for printing surfaces (i.e., green region), which is large enough to cover all parts of all structural members (for interpretation of the references to colour in this figure caption, the reader is referred to the web version of this article).

#### 4.1. Half wheel example

In this example the performance- and printability-based approaches described in Section 3.3.1 are applied to the well-known 'half wheel' optimization problem shown in Fig. 6. To identify printing surfaces, the domain is discretized using  $9 \times 12$  zones of equal size, apart from the central zones that are split into two (see Fig. 11(b)) to address the issue described in Fig. 9(b). Also, the primary build direction is assumed to be vertical and the maximum overhang angle  $\phi_{\text{max}}$  and maximum turning angle  $\phi_{\text{t,max}}$  are both set to 45°.

The initially identified optimal (minimum volume) design shown in Fig. 11(a) is used as a starting point. Results for the printing surface identification step are shown in Fig. 11(b), whilst results for the performance- and printability-based approaches are shown in Fig. 11(c) to (f). In addition, iteration histories for the performance- and printability-based approaches are presented in Fig. 12.

Considering first the performance-based approach, members with initial overhang violations (highlighted in red in Fig. 11(c)) are penalized in Eq. (9). Therefore, in the holistic optimization process, the members affected by the overhang issue gradually shrink in length and the structural volume increases (Fig. 12). The overhang violations are in this case successfully reduced to zero, with the volume of the structure shown in Fig. 11(e) being only 2.57% above that of the reference design shown in Fig. 11(a).

Considering next the printability-based approach, members with overhang violations are removed from the ground structure, with Problem (5) then solved to generate the structure shown in Fig. 11(d), which has a volume that is 3.70% above that of the reference design. In the holistic optimization, as the structural geometry changes, the structural volume gradually decreases (Fig. 12), and a more efficient structural form is obtained together with the associated printing surfaces; see Fig. 11(f), where the volume is reduced to 2.96% above that of the reference design.

In this case it can be observed that the optimized designs and corresponding printing surfaces obtained using the performanceand printability-based approaches are very similar - a phenomenon that is generally not seen when using 3-axis AM machines (e.g., see [31]). Differences exist between the performance- and printability-based structures due to the non-linear and non-convex nature of problem (6), which means that in general only locally optimal solutions are identified.

It is also worth noting that the horizontal member on the top of the structure shown in Fig. 11(a) is the member that most violates the overhang constraints, and that in Fig. 11(b) to (f) the printing surfaces for the top part of the structure are concave. For these concave printing surfaces, the maximum turning angles are restricted by Eq. (3) to avoid the collision problem shown in Fig. 2(c). It is therefore of interest to carry out a parametric study in which the maximum turning angle  $\phi_{t,max}$  is varied, which represents the maximum concave angle permitted by the AM machine to avoid the printing head collision shown in Fig. 2(c). Thus Fig. 13 shows the resulting structures and their associated printing surfaces obtained using the performance-based approach. It can be observed that, as  $\phi_{t,max}$  increases (e.g., for 7-axis AM machines, which have significant flexibility), more efficient structures are generated. For AM machines with lower flexibility (e.g., for 5-axis machines, where  $\phi_{t,max} = 0^{\circ}$ ), a relatively large volume increase of 14.92% is observed (compared with the reference design shown in Fig. 11(a)). Nevertheless, the design is still much more efficient than that obtainable using a 3-axis machine (e.g. 60.4% compliance increase reported in [25]).

#### 4.2. Cantilever example

In this section a cantilever truss example will be used to investigate the influence of primary build direction on the generated optimal designs. This investigation was stimulated by the fact that the choice of primary build direction when using 3-axis AM machines has been found to be of great significance (e.g., in [31] and [42] structural layouts and their associated performance obtained were observed to vary greatly when using different primary build directions).

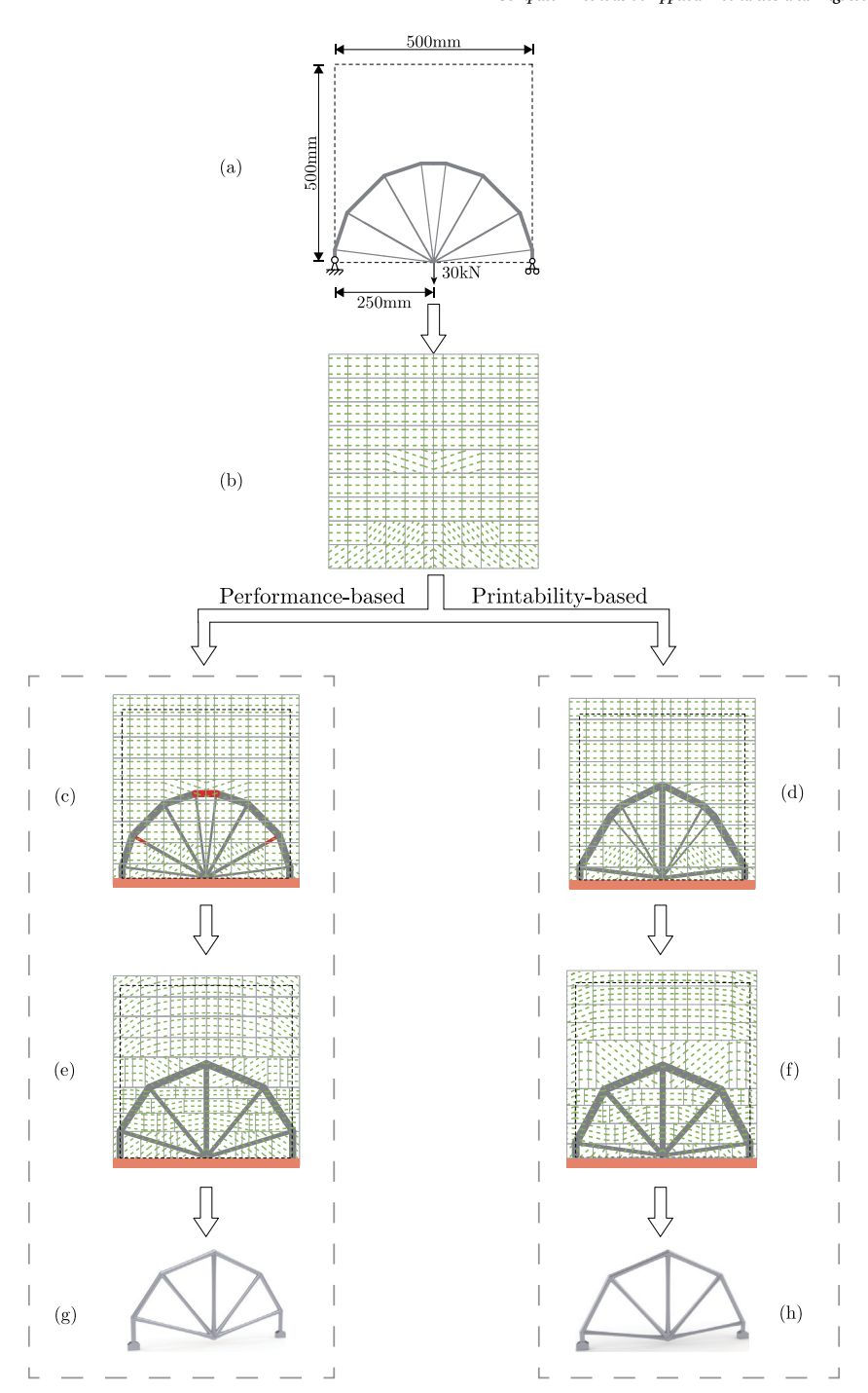


Fig. 11. Half wheel example: (a) optimized structure obtained without considering the overhang problem,  $V = V_0$ ; (b) initial zones and optimized printing surfaces (assuming vertical primary build direction); (c) starting point for the performance-based approach,  $V = V_0$ ; (d) starting point for the printability-based approach,  $V = 1.0370V_0$ ; (e) optimized solution for the performance-based approach,  $V = 1.0257V_0$ ; (f) optimized solution for the printability-based approach,  $V = 1.0296V_0$ ; (g) 3D model of (e); (h) 3D model of (f) (where V is the structural volume; red bars are not printable due to the overhang problem; green dashed lines represent printing surfaces; for interpretation of the references to colour in this figure caption, the reader is referred to the web version of this article).

Details of the cantilever example are shown in Fig. 14(a), with the maximum printable angle  $\phi_{max}$  taken as 45° and the maximum turning angle  $\phi_{t,max}$  taken as 30°. The optimized results with the performance-based approach are shown in Fig. 14(b) to (e). As in the case of the previous example, when using the holistic optimization formulation the initial overhang violations are eliminated in all cases. When using a primary build direction of 90°, only a small volume increase, of less than 1%, is reported, with the resulting

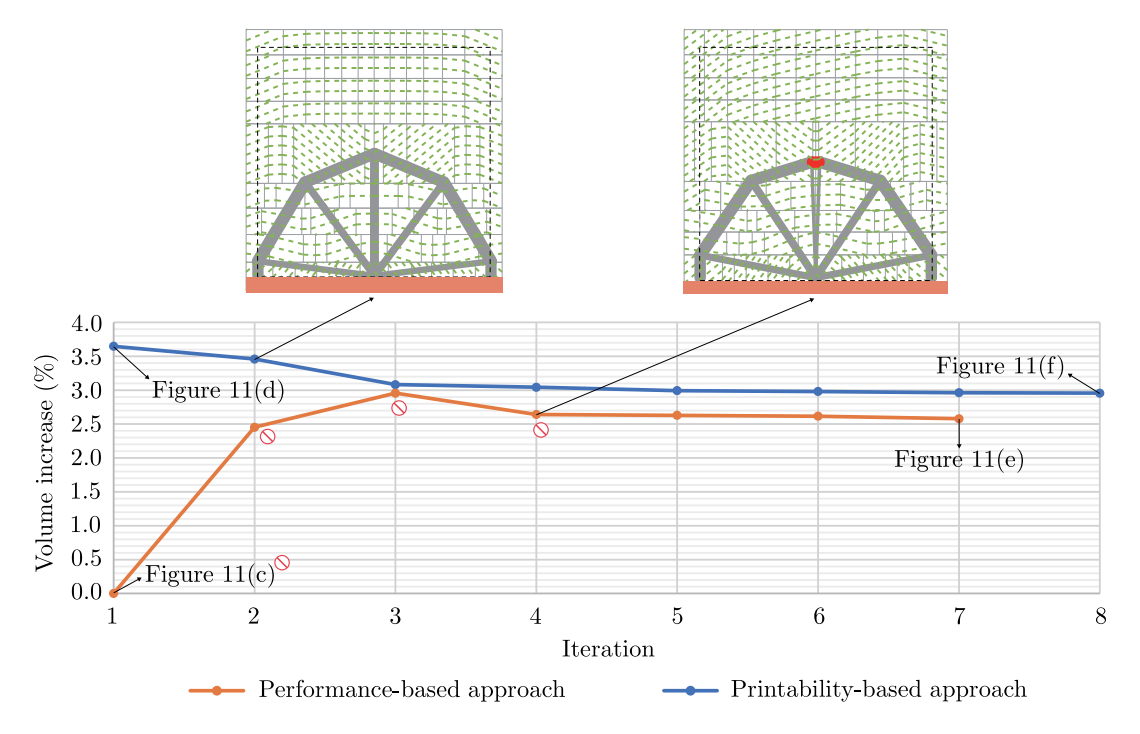


Fig. 12. Half wheel example: iteration history, where the structures in the first four iterations of the performance-based approach are only partly printable (volume increase is relative to the reference design shown in Fig. 11(a); red bars are not printable due to the overhang problem; green dashed lines represent printing surfaces; black dashed lines represent extent of design domain; for interpretation of the references to colour in this figure caption, the reader is referred to the web version of this article).

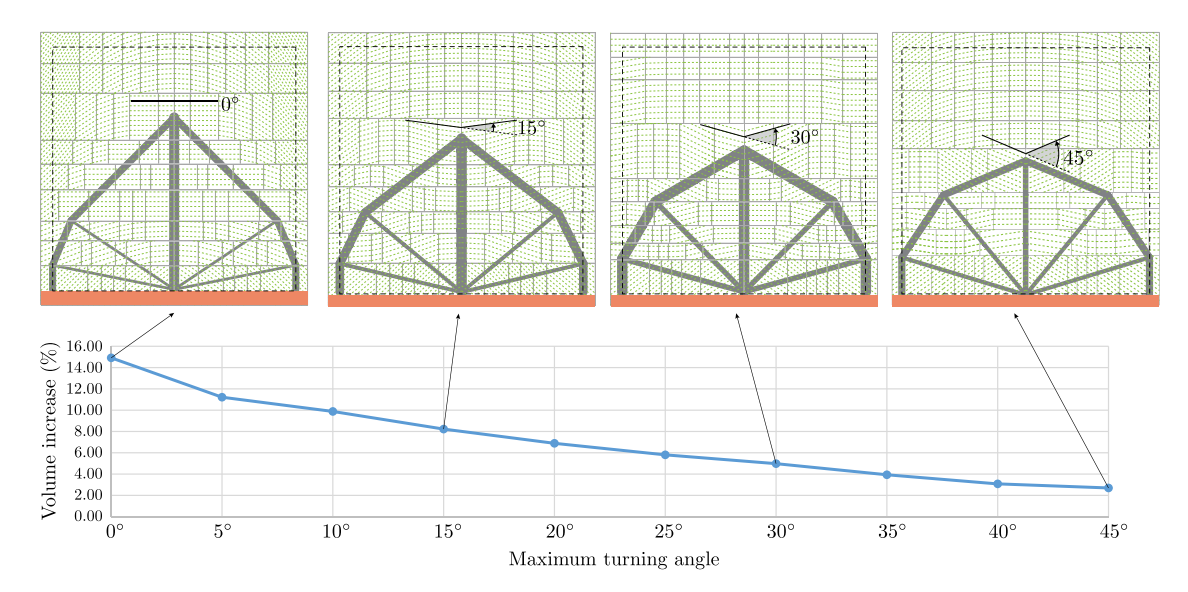
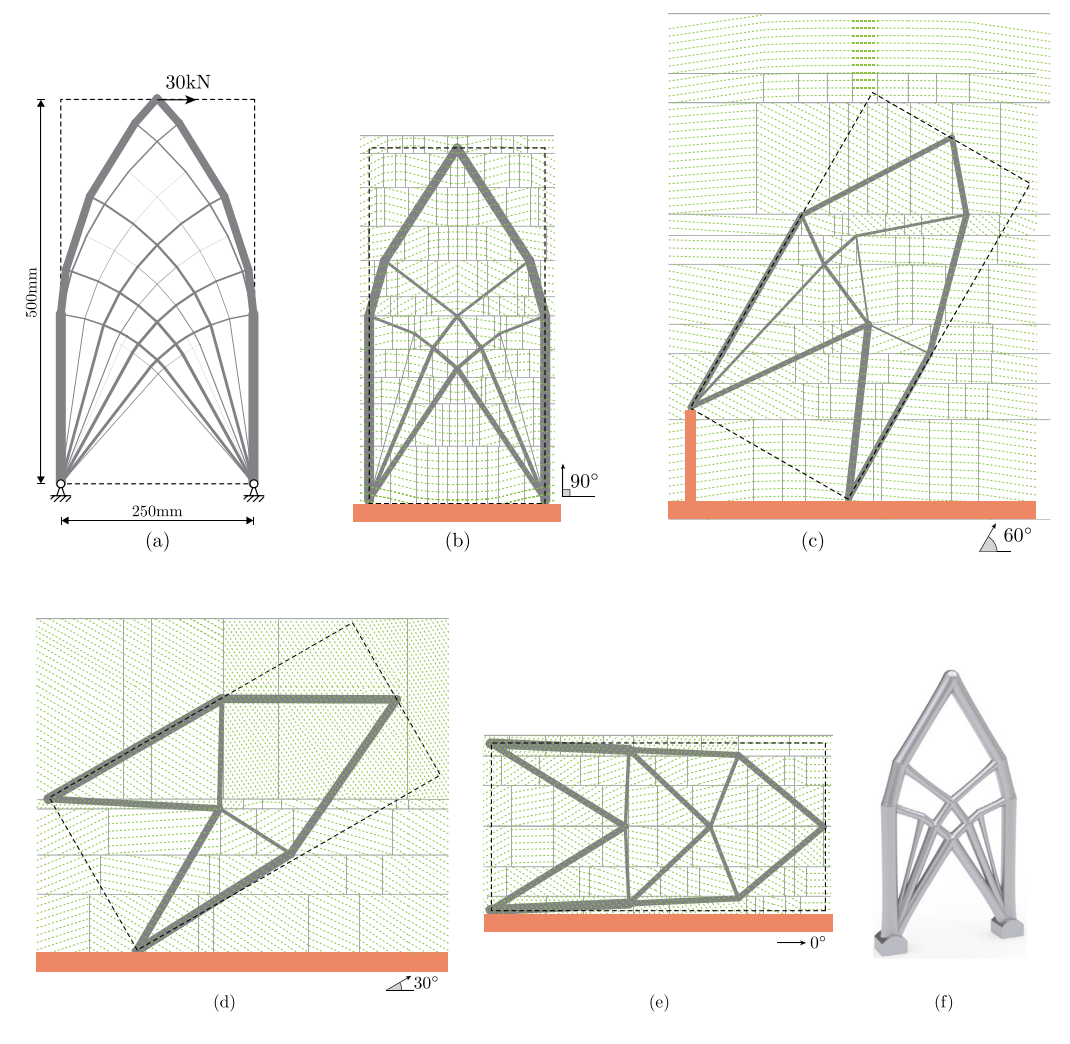


Fig. 13. Half wheel example: relation between volume increase and maximum turning angle (volume increase is relative to the reference design shown in Fig. 11(a); green dashed lines represent printing surfaces; black dashed lines represent extent of design domain; for interpretation of the references to colour in this figure caption, the reader is referred to the web version of this article).

optimized design shown in Fig. 14(b). The volume is then observed to increase slightly as the build direction angle reduces in Fig. 14(c) and (d). The volume increase observed when a build direction of 0° is used (see Fig. 14(e)) is relatively large (8.15% compared to Fig. 14(a)), principly because the top and bottom members are now inclined rather horizontal. However, in comparison in [31] it was found that the volume difference between the most and least favourable build directions when using 3-axis AM was much larger (>50.0%).



**Fig. 14.** Cantilever example: (a) optimized cantilever without overhang constraint considered,  $V = V_0$ ; (b) solution with 90° primary build direction,  $V = 1.0074V_0$ ; (c) solution with 60° primary build direction,  $V = 1.0283V_0$ ; (d) solution with 30° primary build direction,  $V = 1.0440V_0$ ; (e) solution with 0° primary build direction,  $V = 1.0815V_0$ ; (f) 3D model of (b) (where V is the structural volume; green dashed lines represent printing surfaces; for interpretation of the references to colour in this figure caption, the reader is referred to the web version of this article).

It is also worth noting that in some cases the use of a rotated primary build direction may require the presence of an additional support structure to start the print (e.g., see Fig. 14(c)), or may induce a significant bending moment due to the presence of a single point connecting the structure to the base platform (e.g., see Fig. 14(d) and (e)). Therefore, for the problem shown in Fig. 14(a), 90° is also likely to be the best primary build direction for practical reasons.

#### 4.3. MBB beam example

The Messerschmidt–Bölkow–Blohm (MBB) beam is a widely studied example problem; Fig. 15(a) provides details of the particular problem considered herein. The problem has also been investigated in [31], where it was found that the introduction of 3-axis AM printability constraints led to an increase in the volume of the structure of 59%, caused in large part by the fact that the top and bottom members were replaced with self-supporting but inefficient zig-zag elements (Fig. 15(b)). To demonstrate the benefit of manufacturing the same part via a multi-axis machine, the methods proposed in this contribution will now be applied to the problem. Taking advantage of symmetry, only half the domain needs to be considered. The maximum turning angle  $\phi_{t,max}$  is taken as 30°.

Fig. 15(c) shows the design obtained when using the performance-based approach with a maximum overhang angle of 60°. It is evident that there are no overhang violations in this case. However, if the primary build direction is vertical then temporary platforms need to be placed at the bottom left and right corners to enable the printing process to begin, as indicated in the Figure. It can be observed that the volume of the design is only slightly higher than the reference volume (2.42%). Instead of significantly

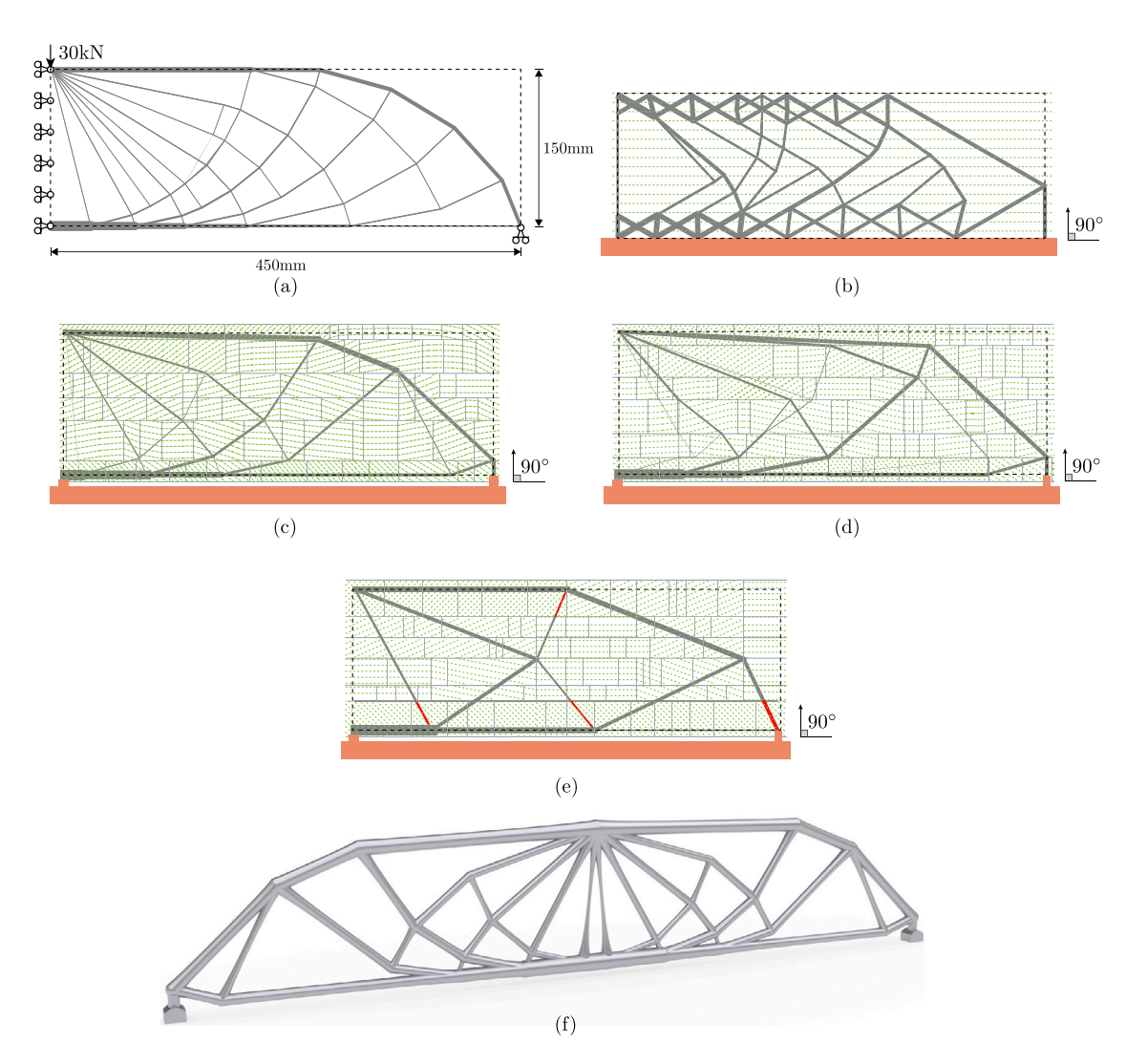


Fig. 15. MBB beam example: (a) optimized structure without overhang constraints considered,  $V = V_0$ ; (b) 3-axis solution with  $\phi_{\text{max}} = 60^\circ$ ,  $V = 1.5900V_0$ ; (c) multi-axis performance-based solution with  $\phi_{\text{max}} = 60^\circ$ ,  $V = 1.0242V_0$ ; (d) multi-axis printability-based solution with  $\phi_{\text{max}} = 45^\circ$ ,  $V = 1.0332V_0$ ; (e) multi-axis performance-based solution with  $\phi_{\text{max}} = 45^\circ$ ,  $V = 1.0310V_0$ ; (f) 3D model of (c) (where  $\phi_{\text{max}}$  is the maximum overhang angle; V is the structural volume; red bars are not printable due to the overhang problem; green dashed lines represent printing surfaces; the primary building direction is perpendicular to the long edge of the design domain in all cases; for interpretation of the references to colour in this figure caption, the reader is referred to the web version of this article).

altering the structural layout, the holistic optimization process can now successfully identify suitable printing surfaces that satisfy the overhang constraints.

When the maximum overhang angle is reduced to  $45^{\circ}$  then the problem becomes more challenging and only the printability-based approach can identify a design with no overhang violations (see Fig. 15(d)), with several violations in evidence when the performance-based approach is used in this case (see Fig. 15(e)). It is also worth noting that the performance-based approach generally leads to identification of structures that are simpler in form than the reference design (e.g., compare the designs shown in Fig. 15(c) and (e) with the design shown in Fig. 15(a)) as the overhang violation in Eq. (9) can be addressed by directly removing violating members (by reducing selected member cross-sectional areas to zero).

#### 4.4. L-shaped cantilever example

In this example, the influence of the maximum overhang angle  $\phi_{max}$  is investigated via use of an L-shaped cantilever example. The design domain, loading and boundary conditions are shown along with the reference solution in Fig. 16(a). The maximum overhang angle  $\phi_{max}$  is varied from 45° to 60° (at or beyond the limit of what can be achieved with current generation processes),

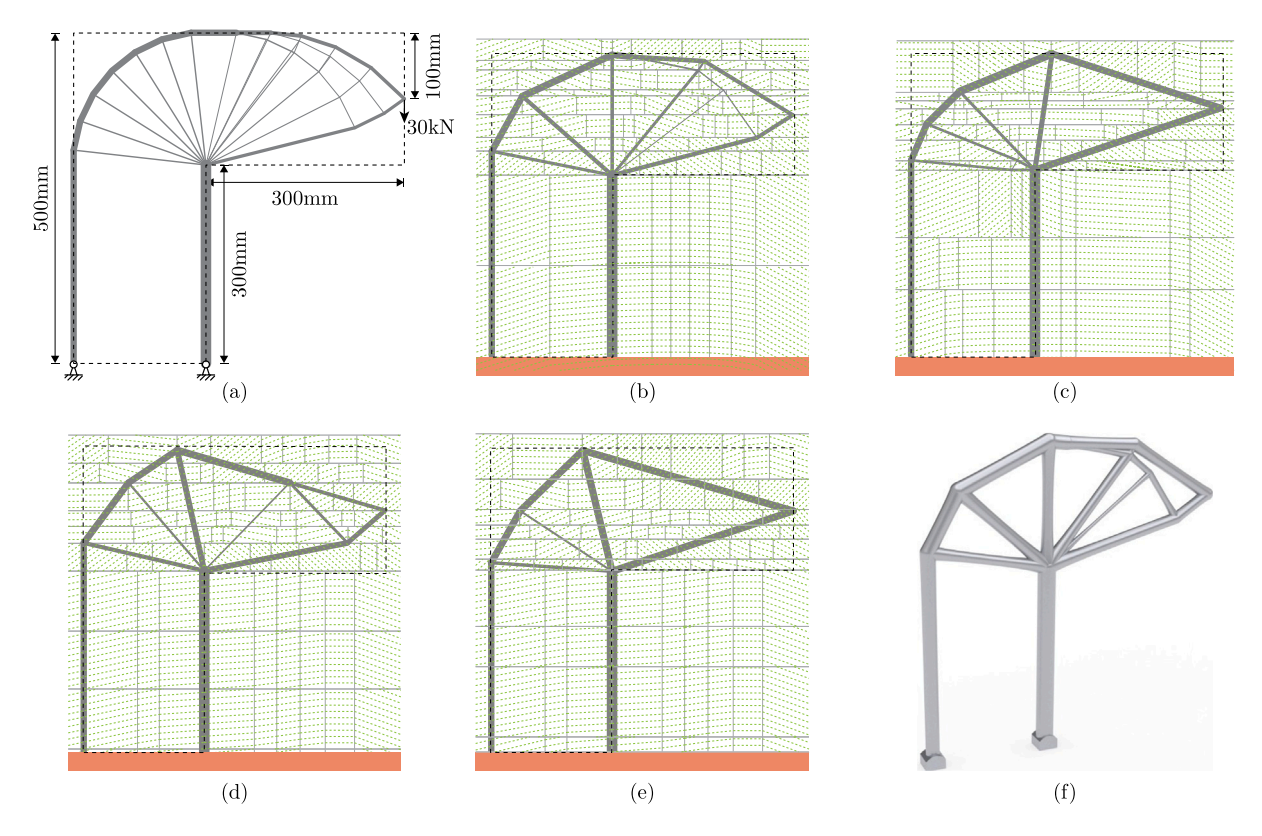


**Fig. 16.** L-shaped cantilever example: (a) optimized cantilever without overhang constraints considered,  $V = V_0$ ; (b) solution with  $\phi_{max} = 60^\circ$ ,  $V = 1.0372V_0$ ; (c) solution with  $\phi_{max} = 55^\circ$ ,  $V = 1.0710V_0$ ; (d) solution with  $\phi_{max} = 50^\circ$ ,  $V = 1.0857V_0$ ; (e) solution with  $\phi_{max} = 45^\circ$ ,  $V = 1.0934V_0$ ; (f) 3D model of (b) (where  $\phi_{max}$  is the maximum overhang angle; V is the structural volume; green dashed lines represent printing surfaces; for interpretation of the references to colour in this figure caption, the reader is referred to the web version of this article).

with the maximum turning angle  $\phi_{t,max}$  set at 30°. The resulting optimized designs obtained when using the performance-based approach are shown in Fig. 16(b) to (e).

Fig. 16 shows that the structural volume increases as  $\phi_{max}$  decreases, since smaller  $\phi_{max}$  values correspond to increasing overhang limitations. The associated changes in structural form are also evident. It can also be observed from Fig. 16(a) that the most difficult part of the reference design to reproduce is the horizontal member at the top of the domain, which is instead represented by a series of inclined members in Fig. 16(b) to (e) to overcome the overhang problem.

#### 4.5. MX3D cantilever example

In this example a cantilever structure recently designed using the Peregrine layout optimization plugin [43] for the Rhino/Grasshopper parametric design software is considered. After the initial optimization, post-processing routines developed at Imperial College London were applied to ensure compliance with codes of practice, prior to the structure being fabricated by MX3D using the wire arc additive manufacturing technique (WAAM). The cantilever is a relatively large structural element comprising tubular elements and was designed to evaluate the potential for additive manufacturing to be used in the construction sector; further details of the design and manufacture process for this structure are outlined in Ye et al. [44]. Note that the first cantilever fabricated was decomposed into separately manufactured sections that were then manually welded together. In this contribution the methods described previously will be used to develop a single step manufacturing scheme, thereby avoiding the need for labour-intensive manual assembly steps (note that a second cantilever was subsequently successfully manufactured in a single step).

A description of the design problem and also selected details of the optimized structure considered by Ye et al. [44] are shown in Fig. 17. The material used was a carbon steel with a stress limit of 458 MPa. To overcome the overhang problem, printing surfaces were manually identified; e.g. see Fig. 17(b). Even though the structure is relatively simple, and contains relatively few joints, a total of 12 zones were used to manufacture the small region shown in Fig. 17(b) (this was to both maintain appropriate printing orientations and to avoid collisions). It thus quickly becomes challenging to develop manufacturing schemes for larger, more complex designs.

Here the maximum overhang angle and turning angle are set to  $45^{\circ}$  and  $30^{\circ}$  respectively. Rather than solving Problem (5), here the structural layout shown in Fig. 17(a) is used as a starting point. The domain is discretized with  $12 \times 20$  zones (see Fig. 18(a)),

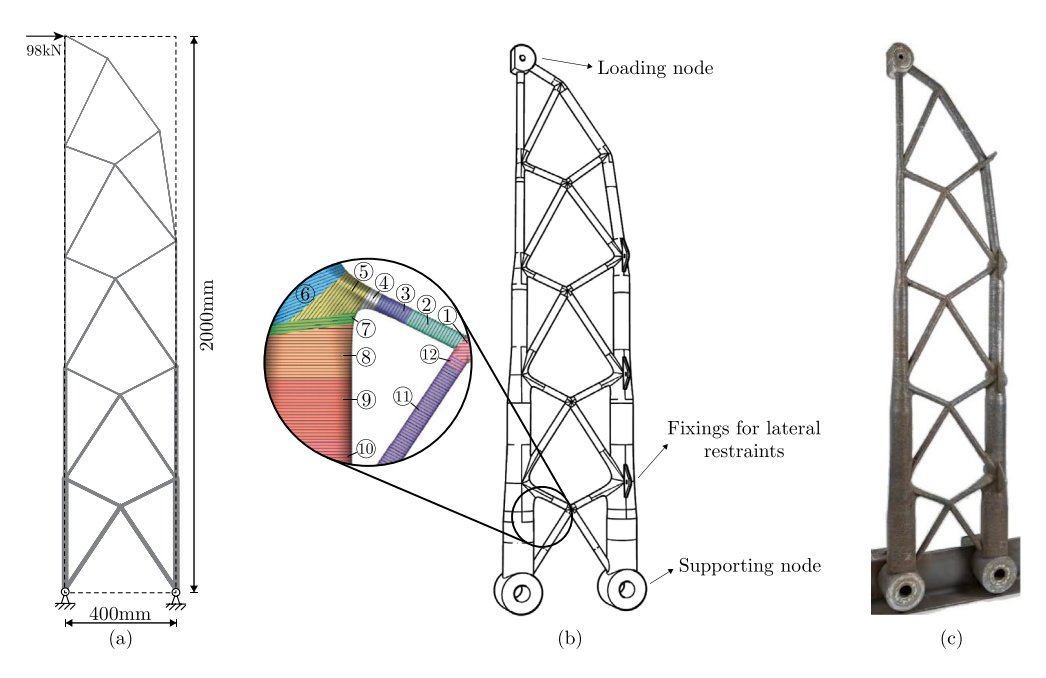


Fig. 17. MX3D cantilever example: (a) optimized structural layout; (b) 3D model, where the region highlighted includes 12 manually selected zones, each with different printing surfaces; (c) manufactured cantilever using WAAM (all after [44]).

with horizontal zone boundaries placed to coincide with joints. Suitable printing surfaces are then identified by solving Eq. (4); see Fig. 18(a). Note that as the structure depicted in Fig. 17(a) had already been optimized via geometry optimization by Ye et al. [44], the structural layout remains the same after the holistic optimization process has been performed.

Once details of the 3D model and associated printing surfaces are available, the corresponding tool path can be obtained automatically via a geometry intersection operation; see Fig. 18(b). Note that in this case the tool path only needed to be created for the main cantilever element, as the loading and support ring were to be manufactured separately; see [44]. The tool path was validated using the manufacturing simulation software VERICUT [45], with a multi-axis metal DED machine used to manufacture the component virtually. This showed that no collisions occurred during the entire manufacturing process, thereby demonstrating the manufacturability of the design. A video of the printing simulation is provided as electronic supplementary material (see 'Data availability' section for details of how to access this).

#### 4.6. Vertical 3D cantilever example

Although the algorithms for generating printing surfaces outlined in Sections 2 and 3 were described in the context of 2D design problems, the same concept can be applied to 3D problems. Instead of utilizing line segments to represent curves (e.g., see Fig. 2), 3D printing surfaces can be approximated via piecewise facets. To demonstrate this a simple 3D example problem is shown in Fig. 19, with the maximum overhang angle and turning angles set to  $45^{\circ}$  and  $30^{\circ}$  respectively. For sake of simplicity, the design domain is split into five 'floors', each discretized with  $20 \times 20$  equally sized zones.

The optimized structure and corresponding printing surfaces are shown in Fig. 19(b). The 3D model was created using the approach described in [35]. The tool path was generated by slicing the 3D model using the identified printing surfaces; see Fig. 19(c). The printability of the design was confirmed using the manufacturing simulation software VERICUT, using the same settings as for the MX3D cantilever described in Section 4.5, with no collisions detected during the entire manufacturing process. A video of the printing simulation is provided as electronic supplementary material (see 'Data availability' section for details of how to access this).

#### 4.7. Commentary

Table 1 shows volume increases arising from the presence of overhang constraints for all examples considered in Section 4. Note that all solutions shown are fully self-supporting (i.e., have no overhang violations). It is evident that in most cases the volume increases observed when using multi-axis AM are less than 10%. In the cases of the MX3D and vertical 3D cantilever examples described in Sections 4.5 and 4.6, since it was possible to identify printing surfaces with no overhang violation without modifying the structural layout, the reported volume increases are 0%. For the MBB beam example described in Section 4.3, when the solution was compared with that obtained using a previously described 3-axis AM approach, it was found that the use of multi-axis AM led to a significant reduction in the volume increase arising from the introduction of manufacturing constraints, from 59% to 2.42%.

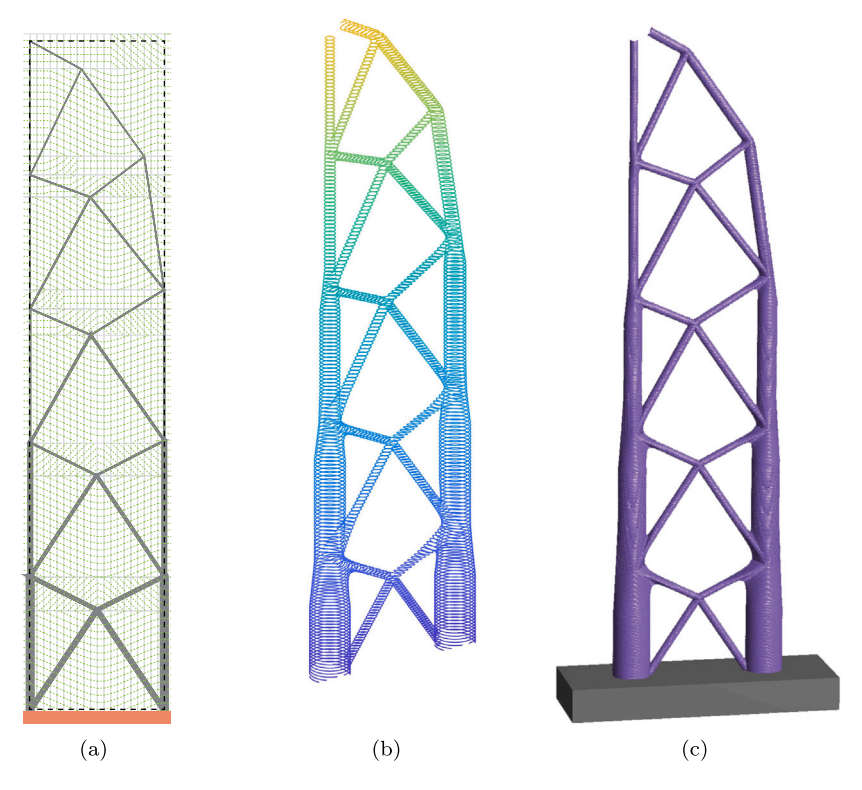


Fig. 18. MX3D cantilever example: (a) printing surfaces obtained using  $12 \times 20$  zones (vertical zone boundaries hidden for clarity); (b) tool path, showing large (10 mm) layer thickness for clarity; (c) virtually manufactured model using AM simulation software VERICUT (black dashed lines represent structural design domain; the support and loading rings, and the lateral restraint fixings indicated in Fig. 17(b), have been omitted).

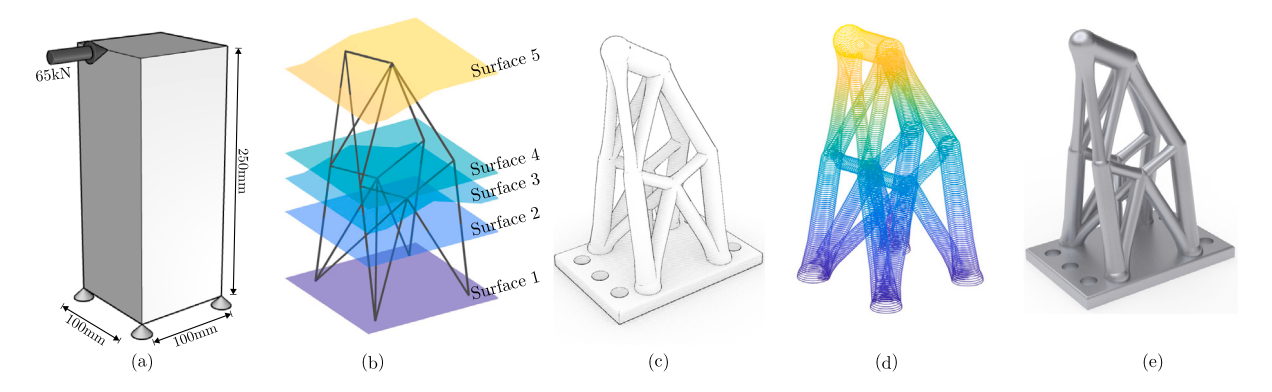


Fig. 19. 3D cantilever example: (a) case description; (b) optimized structure and printing surfaces; (c) 3D model of the optimized cantilever; (d) automatically sliced tool path (validated via VERICUT simulation); (e) photorealistic image of the optimized space-truss cantilever.

In other words, the proposed multi-axis AM design approach is capable of identifying optimized designs that have high printability and performance.

CPU times for all the examples described herein are presented in Table 1, obtained using a laptop PC running Microsoft Windows 10 equipped with an AMD 5900HX CPU. Note that in each case the reported CPU time only includes the time required for printing surface identification (i.e., solving Problem (4)) and holistic optimization (i.e., solving Problem (6)); the time spent on identifying an initial optimized structure is not included since Problem (5) can be solved very efficiently using e.g., the well-established adaptive 'member adding' approach [34]. It is evident from the table that the computational cost is relatively low in all cases, confirming the high computational efficiency of the proposed approach. Most of the computational cost is associated with solving the nonconvex holistic optimization problem and, in examples where a holistic optimization is not required (i.e., the examples described in Sections 4.5 and 4.6), the total computational cost is very low.

**Table 1** Volume increases ( $\Delta V$ ) caused by the overhang constraint for all examples considered in Section 4 (where  $\phi_{\max}$  is the maximum overhang angle;  $\phi_{t,\max}$  is the maximum turning angle; note that multi-axis AM machines with greater flexibility have higher  $\phi_{\max}$  and  $\phi_{t,\max}$  values; for the 3-axis AM machine  $\phi_{t,\max} = 0$ ).

	3-axis AM		Multi-axis AM				
	$\phi_{ m max}$	$\Delta V$	$\phi_{t,max}$	$\phi_{ m max}$	Build direction	CPU time (sec)	ΔV
Half wheel (Section 4.1.1)	-	-	0°	45°	90°	52.48	14.92%
	-	-	15°	45°	90°	71.78	8.23%
	-	-	30°	45°	90°	73.92	5.14%
	-	-	45°	45°	90°	45.23	2.57%
Cantilever (Section 4.2)	-	-	45°	45°	90°	44.53	0.74%
	-	-	45°	45°	60°	121.67	2.83%
	-	-	45°	45°	30°	111.71	4.40%
	-	-	45°	45°	0°	88.40	8.15%
MBB beam (Section 4.3)	60°	59.00%	30°	60°	90°	78.73	2.42%
	-	-	30°	45°	90°	90.80	3.32%
L-shaped cantilever (Section 4.4)	-	-	30°	60°	90°	63.25	3.72%
	-	-	30°	55°	90°	68.26	7.10%
	-	-	30°	50°	90°	75.15	8.57%
	-	-	30°	45°	90°	55.52	9.34%
MX3D cantilever (Section 4.5)	-	-	30°	45°	90°	0.148	0%
Vertical 3D cantilever (Section 4.6)	-	-	30°	45°	90°	0.268	0%

When considering multi-axis AM, ideally both the primary and local build directions shown in Fig. 2 should be able to be varied in the optimization. However, in this study the primary build direction has been assumed to be fixed (and perpendicular to the base platform), with only the local build directions treated as variables. While this might appear to greatly restrict the flexibility of the multi-axis AM process employed, and hence also the optimality of the structural forms generated, the benefit in terms of numerical efficiency is significant. This is because the assumption greatly simplifies the printing surface identification problem, making Problem (4) linear. This is reflected in the relatively low CPU times presented in Table 1. The high numerical efficiency of the presented approach makes it possible to explore a number of primary directions in order to determine the most favourable one, as illustrated in Section 4.2. Furthermore, in relation to structural efficiency, the presented examples suggest that the impact of constraining the primary build direction will often be negligible; e.g., from Table 1 it is clear that the increases in volume due to the overhang constraint are relatively small. Thus, the benefits of restricting the primary build direction appear to outweigh the drawbacks.

In addition to the overhang problem considered in the present work, research indicates that, due to the anisotropic nature of additively manufactured materials, optimal mechanical properties are usually achieved when the printing nozzle remains perpendicular to already printed elements [46,47]. While the current formulation does not seek to take account of this, should the requisite material property data be available, the formulation could readily be modified to model reduced strength properties in non-perpendicular members. Also, in the present work, the approach has only been applied to one, relatively simple, 3D problem. An area of future work is to apply the proposed approach (described in Section 3.3) to a range of more complex 3D problems, though, due to the nature of the underlying problem formulation, this will significantly increase the computational cost.

#### 5. Conclusions

A novel holistic optimization approach has been proposed that allows simultaneous identification of minimum volume truss structures and their associated curved printing surfaces for use with multi-axis additive manufacturing (AM) machines. In the optimization process, local build directions for the curved printing surfaces are defined using a zone decomposition method. Starting with a regular zone grid, a holistic optimization approach is used to automatically adjust the sizes and positions of zones, and to define local build directions for the resulting optimized structure. Due to the non-linear and non-convex nature of the underlying optimization problem, two strategies have been proposed:

- A performance-based approach, in which standard numerical layout optimization is used to generate (near-) optimal truss structures that may include overhang violations, which are then reduced or eliminated by simultaneously adjusting the structural form and the associated printing surfaces.
- A printability-based approach, in which members violating overhang constraints are removed from the ground structure, ensuring that the subsequently identified optimized structures, obtained by simultaneously adjusting the structural form and the associated printing surfaces, are overhang-free.

The effectiveness of the above approaches has been demonstrated via application to various 2D and 3D example problems. When using the performance-based approach it was observed that overhang violations could often be completely eliminated using the proposed holistic optimization approach. Also, when using the printability-based approach, it was observed that the structural performance of an initial design without overhang violations could be significantly improved upon.

Although the non-linear, non-convex optimization formulation involved means that only locally optimal solutions are obtainable, the optimality of the designs generated can be appraised by comparing their volumes with those of reference solutions obtained without imposing overhang constraints. It is evident that using multi-axis rather than 3-axis AM processes for design problems involving overhang constraints will often lead to much smaller volume increases. For instance, in the case of one of the examples considered in this study, the increase when using multi-axis AM was found to be 2.4%, compared to 59.0% when using 3-axis AM.

#### Declaration of competing interest

The authors declare that they have no known competing financial interests or personal relationships that could have appeared to influence the work reported in this paper.

#### Data availability

Videos of the printing simulations prepared for the MX3D and 3D cantilever examples are available at: https://doi.org/10.15131/shef.data.22559578 (see files Suppl\_Video1.mp4 and Suppl\_Video2.mp4 respectively).

#### Acknowledgements

This research was made possible by funding from the European Union's Horizon 2020 research and innovation programme under grant agreement No. 820776 'Intelligent data-driven pipeline for the manufacturing of certified metal parts through Direct Energy Deposition process (INTEGRADDE)'.

#### References

- [1] K. Vartanian, L. Brewer, K. Manley, T. Cobbs, Powder Bed Fusion vs. Directed Energy Deposition Benchmark Study: Mid-Size Part with Simple Geometry, Optomec, Tech. Rep. 1, 2016.
- [2] B. Liu, H. Shen, Z. Zhou, J. Fu, et al., Research on support-free WAAM based on surface/interior separation and surface segmentation, J. Mater Process. Technol. (2021) 117240.
- [3] T. DebRoy, T. Mukherjee, J. Milewski, J. Elmer, B. Ribic, J. Blecher, W. Zhang, Scientific, technological and economic issues in metal printing and their solutions, Nature Mater. 18 (10) (2019) 1026–1032.
- [4] Y. Oh, C. Zhou, S. Behdad, Part decomposition and assembly-based (Re) design for additive manufacturing: A review, Addit. Manuf. 22 (2018) 230-242.
- [5] Y. Gao, L. Wu, D.-M. Yan, L. Nan, Near support-free multi-directional 3D printing via global-optimal decomposition, Graph. Models 104 (2019) 101034.
- [6] C. Wu, C. Dai, G. Fang, Y.-J. Liu, C.C. Wang, General support-effective decomposition for multi-directional 3-D printing, IEEE Trans. Autom. Sci. Eng. 17 (2) (2019) 599-610.
- [7] E. Karasik, R. Fattal, M. Werman, Object partitioning for support-free 3D-printing, Comput. Graph. Forum 38 (2) (2019) 305–316.
- [8] C. Dai, C.C. Wang, C. Wu, S. Lefebvre, G. Fang, Y.-J. Liu, Support-free volume printing by multi-axis motion, ACM Trans. Graph. 37 (4) (2018) 1-14.
- [9] K. Xu, Y. Li, L. Chen, K. Tang, Curved layer based process planning for multi-axis volume printing of freeform parts, Comput. Aided Des. 114 (2019) 51–63.
- [10] Y. Li, D. He, X. Wang, K. Tang, Geodesic distance field-based curved layer volume decomposition for multi-axis support-free printing, 2020, arXiv preprint arXiv:2003.05938.
- [11] F. Xie, X. Jing, C. Zhang, S. Chen, D. Bi, Z. Li, D. He, K. Tang, Volume decomposition for multi-axis support-free and gouging-free printing based on ellipsoidal slicing, Comput. Aided Des. 143 (2022) 103135.
- [12] Y. Li, D. He, S. Yuan, K. Tang, J. Zhu, Vector field-based curved layer slicing and path planning for multi-axis printing, Robot. Comput.-Integr. Manuf. 77 (2022) 102362.
- [13] O. Sigmund, A 99 line topology optimization code written in Matlab, Struct. Multidiscipl. Optim. 21 (2) (2001) 120–127, http://dx.doi.org/10.1007/s001580050176.
- [14] Y. Zhou, K. Saitou, Gradient-based multi-component topology optimization for additive manufacturing (MTO-A), in: IDETC/CIE, Vol. 58127, American Society of Mechanical Engineers, 2017, V02AT03A033.
- [15] M. Langelaar, Topology optimization of 3D self-supporting structures for additive manufacturing, Addit. Manuf. 12 (2016) 60-70.
- [16] M. Langelaar, An additive manufacturing filter for topology optimization of print-ready designs, Struct. Multidiscipl. Optim. 55 (3) (2017) 871-883.
- [17] A.T. Gaynor, J.K. Guest, Topology optimization considering overhang constraints: Eliminating sacrificial support material in additive manufacturing through design, Struct. Multidiscipl. Optim. 54 (5) (2016) 1157–1172.
- [18] Y.-H. Kuo, C.-C. Cheng, Self-supporting structure design for additive manufacturing by using a logistic aggregate function, Struct. Multidiscipl. Optim. 60 (3) (2019) 1109–1121.
- [19] T.E. Johnson, A.T. Gaynor, Three-dimensional projection-based topology optimization for prescribed-angle self-supporting additively manufactured structures, Addit. Manuf. 24 (2018) 667–686.

- [20] X. Qian, Undercut and overhang angle control in topology optimization: a density gradient based integral approach, Internat. J. Numer. Methods Engrg. 111 (3) (2017) 247–272.
- [21] A. Garaigordobil, R. Ansola, J. Santamaría, I.F. De Bustos, A new overhang constraint for topology optimization of self-supporting structures in additive manufacturing. Struct. Multidiscipl. Optim. 58 (5) (2018) 2003–2017.
- [22] E. van de Ven, R. Maas, C. Ayas, M. Langelaar, F. van Keulen, Continuous front propagation-based overhang control for topology optimization with additive manufacturing, Struct. Multidiscipl. Optim. 57 (5) (2018) 2075–2091.
- [23] E. van de Ven, R. Maas, C. Ayas, M. Langelaar, F. van Keulen, Overhang control in topology optimization: a comparison of continuous front propagation-based and discrete layer-by-layer overhang control, Struct. Multidiscipl. Optim. 64 (2) (2021) 1–18.
- [24] C. Wang, Simultaneous optimization of build orientation and topology for self-supported enclosed voids in additive manufacturing, Comput. Methods Appl. Mech. Engrg. 388 (2022) 114227.
- [25] G. Allaire, C. Dapogny, R. Estevez, A. Faure, G. Michailidis, Structural optimization under overhang constraints imposed by additive manufacturing technologies, J. Comput. Phys. 351 (2017) 295–328.
- [26] Y. Wang, J. Gao, Z. Kang, Level set-based topology optimization with overhang constraint: Towards support-free additive manufacturing, Comput. Methods Appl. Mech. Engrg. 339 (2018) 591–614.
- [27] W. Zhang, L. Zhou, Topology optimization of self-supporting structures with polygon features for additive manufacturing, Comput. Methods Appl. Mech. Engrg. 334 (2018) 56–78.
- [28] M. Bi, P. Tran, Y.M. Xie, Topology optimization of 3D continuum structures under geometric self-supporting constraint, Addit. Manuf. 36 (2020) 101422.
- [29] X. Guo, J. Zhou, W. Zhang, Z. Du, C. Liu, Y. Liu, Self-supporting structure design in additive manufacturing through explicit topology optimization, Comput. Methods Appl. Mech. Engrg. 323 (2017) 27–63.
- [30] Y. Mass, O. Amir, Topology optimization for additive manufacturing: Accounting for overhang limitations using a virtual skeleton, Addit. Manuf. 18 (2017) 58–73.
- [31] L. He, M. Gilbert, T. Johnson, T. Pritchard, Conceptual design of AM components using layout and geometry optimization, Comput. Math. with Appl. 78 (7) (2019) 2308–2324.
- [32] W.S. Dorn, R.E. Gomory, H.J. Greenberg, Automatic design of optimal structures, J. Mec. 3 (1) (1964) 25-52.
- [33] M. Gilbert, A. Tyas, Layout optimization of large-scale pin-jointed frames, Eng. Comput. 20 (8) (2003) 1044-1064.
- [34] L. He, M. Gilbert, X. Song, A python script for adaptive layout optimization of trusses, Struct. Multidiscipl. Optim. 60 (2) (2019) 835-847.
- [35] C.J. Smith, M. Gilbert, I. Todd, F. Derguti, Application of layout optimization to the design of additively manufactured metallic components, Struct. Multidiscipl. Optim. 54 (5) (2016) 1297–1313.
- [36] T. Zegard, G.H. Paulino, Bridging topology optimization and additive manufacturing, Struct. Multidiscipl. Optim. 53 (1) (2016) 175-192.
- [37] L. He, M. Gilbert, Rationalization of trusses generated via layout optimization, Struct. Multidiscipl. Optim 52 (4) (2015) 677-694.
- [38] MOSEK ApS, MOSEK optimizer API for Python. Version 9.3.6, 2019, URL: https://docs.mosek.com/latest/pythonapi/index.html.
- [39] R.T. Haftka, Z. Gürdal, Elements of Structural Optimization, Vol. 11, Springer Science & Business Media, 2012.
- [40] A. Wächter, L.T. Biegler, On the implementation of an interior-point filter line-search algorithm for large-scale nonlinear programming, Math. Program. 106 (1) (2006) 25–57.
- [41] B. Michel, C.M. Uang, R. Sabelli, Ductile Design of Steel Structures, McGraw-Hill Education, 2011.
- [42] C. Wang, X. Qian, Simultaneous optimization of build orientation and topology for additive manufacturing, Addit. Manuf. 34 (2020) 101246.
- [43] L. He, Q. Li, M. Gilbert, P. Shepherd, C. Rankine, T. Pritchard, V. Reale, Optimization-driven conceptual design of truss structures in a parametric modelling environment, Structures 37 (2022) 469–482.
- [44] J. Ye, P. Kyvelou, F. Gilardi, H. Lu, M. Gilbert, L. Gardner, An end-to-end framework for the additive manufacture of optimized tubular structures, IEEE Access 9 (2021) 165476–165489.
- [45] CGTech, VERICUT, 2018, URL: https://cgtech.com/.
- [46] N. Hadjipantelis, B. Weber, C. Buchanan, L. Gardner, Description of anisotropic material response of wire and arc additively manufactured thin-walled stainless steel elements, Thin-Walled Struct. 171 (2022) 108634.
- [47] L. Gardner, Metal additive manufacturing in structural engineering-review, advances, opportunities and outlook, Structures 47 (2023) 2178-2193.